Antecedent North Pacific Jet Regimes Conducive to the Development of Continental U.S. Extreme Temperature Events during the Cool Season

By

ANDREW C. WINTERS[1*], LANCE F. BOSART[1], and DANIEL KEYSER[1]

[1]Department of Atmospheric and Environmental Sciences
University at Albany, State University of New York
Albany, NY 12222

Submitted for publication in *Weather and Forecasting*
XX September 2018

---

[*] *Corresponding author address:* Andrew C. Winters, Dept. of Atmospheric and Environmental Sciences, University at Albany, SUNY, 1400 Washington Ave., Albany, NY 12222. E-mail: acwinters@albany.edu

ABSTRACT

This study considers the development of continental U.S. extreme temperature events (ETEs) during the cool season (Sep–May), where extreme temperatures are defined in terms of percentiles and events are defined in terms of the spatial coverage of extreme temperatures. Following their identification, ETEs are classified into geographic clusters and stratified based on the state of the North Pacific jet (NPJ) stream prior to ETE initiation using an NPJ Phase Diagram. The NPJ Phase Diagram is developed from the two leading modes of NPJ variability during the cool season. The first mode corresponds to a zonal extension or retraction of the exit region of the climatological NPJ, while the second mode corresponds to a poleward or equatorward shift of the exit region of the climatological NPJ.

The projection of 250-hPa zonal wind anomalies onto the NPJ Phase Diagram prior to the occurrence of ETEs provides an objective characterization of the state and evolution of the upper-tropospheric flow pattern over the North Pacific, and demonstrates that the preferred state and evolution of the NPJ prior to ETEs varies considerably based on the location of ETE initiation and meteorological season. The NPJ Phase Diagram is employed further to examine a synoptic-scale flow evolution highly conducive to the initiation of southern Plains extreme warm events via composite analysis. The composite analysis demonstrates that a retracted NPJ supports an amplification of the upper-tropospheric flow pattern over North America, which subsequently induces persistent lower-tropospheric warm-air advection over the southern Plains prior to ETE initiation.

1. Introduction

The occurrence of extreme temperature events (ETEs) during the cool season (Sep–May) is often accompanied by considerable societal and economic impacts. Extreme cold events, in particular, are responsible for about 30 deaths per year in the United States (NWS 2018), can result in substantial damage to infrastructure (e.g., Cellitti et al. 2006), and can induce agricultural and economic losses (e.g., Rogers and Rohli 1991; Gu et al. 2008; Dole et al. 2014; Wolter et al. 2015). While extreme warm events during the cool season have received less consideration within the refereed literature, they also pose considerable risks. These risks include the development of floods and ice jams on waterways due to rapid snow and ice melt (Westby et al. 2013), economic losses for industries reliant upon wintry conditions (Westby et al. 2013), and the potential loss of early season agricultural products when an extreme warm event is followed by a hard freeze (e.g., Rogers and Rohli 1991; Gu et al. 2008; Westby et al. 2013; Dole et al. 2014; Peterson and Abatzoglou 2014; Westby and Black 2015).

From a climatological perspective, the development of one or several ETEs during a single season can contribute disproportionately to temperature anomaly statistics for that particular season (e.g., Hoerling et al. 2013; Peterson et al. 2013; Dole et al. 2014; Hartmann 2015; Wolter et al. 2015). The disproportionate contribution of ETEs to seasonal temperature anomaly statistics suggests that ETEs need to be considered in order to understand the dynamical and thermodynamic processes that operate at the weather–climate intersection. Such investigations of ETEs are of additional importance given projected changes in the frequency of ETEs within future climates (e.g., Walsh et al. 2001; Meehl and Tebaldi 2004; Portis et al. 2006; Vavrus et al. 2006; Peterson et al. 2013; Westby et al. 2013; Scherer and Diffenbaugh 2014; Grotjahn et al. 2016).

Numerous studies have sought relationships between cool season ETEs over North America and modes of intraannual climate variability as part of an effort to understand the large-scale meteorological patterns associated with the development of ETEs (Table 1). For example, prior work has identified relationships between ETEs and the phase of the Pacific–North American pattern (PNA), the North Atlantic Oscillation (NAO), the Arctic Oscillation (AO), and the Madden–Julian Oscillation (MJO). Cool season ETEs have also been related to modes of interannual climate variability such as the phase of the Pacific Decadal Oscillation (PDO) and the El Niño–Southern Oscillation (ENSO). Subseasonal and seasonal forecasts of ETEs, in particular, benefit considerably from knowledge of these relationships.

In addition to intraannual and interannual modes of climate variability, Loikith and Broccoli (2014) emphasize that the synoptic-scale flow pattern also plays an important role in the development of ETEs, especially during the boreal winter. In particular, regional case studies and composite analyses of cool season ETEs over North America have identified attributes of the synoptic-scale flow pattern that are often associated with the development of ETEs. Common attributes among these studies include an amplified upper-tropospheric flow pattern over North America (e.g., Dallavalle and Bosart 1975; Hartjenstein and Bleck 1991; Colle and Mass 1995; Konrad 1996; Cellitti et al. 2006; Loikith and Broccoli 2012; Westby and Black 2015; Xie et al. 2017), the development of surface cyclones and anticyclones that facilitate the transport of anomalous cold or warm air into a region (e.g., Dallavalle and Bosart 1975; Colucci and Davenport 1987; Konrad and Colucci 1989; Colle and Mass 1995; Konrad 1996; Walsh et al. 2001; Westby and Black 2015; Grotjahn and Zhang 2017; Xie et al. 2017), and topographical processes such as cold-air damming (e.g., Bell and Bosart 1988; Hartjenstein and Bleck 1991; Colle and Mass 1995) and the adiabatic warming of air parcels induced by lee subsidence (e.g., Brewer et al. 2012, 2013). Thermodynamic factors such as antecedent precipitation and soil moisture (e.g., Turner and Gyakum 2011; Brewer et al. 2013; Hoerling et al. 2013; Dole et al. 2014), as well as adiabatic and diabatic processes occurring along air parcel trajectories in the absence of topography (e.g., Konrad and Colucci 1989; Walsh et al. 2001; Portis et al, 2006; Turner and Gyakum 2011) can also contribute to the development of ETEs.

While the synoptic-scale flow patterns associated with cool season ETEs feature common attributes, it is apparent that the structure and evolution of these flow patterns are highly dependent on the location of the ETE and the meteorological season (e.g., Loikith and Broccoli 2012, 2014; Westby et al. 2013; Westby and Black 2015; Grotjahn et al. 2016; Grotjahn and Zhang 2017; Loikith et al. 2017; Xie et al. 2017). On the basis of these relationships, Grotjahn et al. (2016) recommend in their review of large-scale meteorological patterns associated with ETEs that additional work be conducted to (1) to determine whether more than one type of large-scale meteorological flow pattern is conducive to the development of ETEs in a particular geographic region, and (2) to increase understanding of the synoptic-dynamic mechanisms that support the development of large-scale meteorological flow patterns associated with ETEs. These two recommendations motivate the present study.

Case studies of extreme weather events (EWEs) over North America demonstrate that the state and evolution of the North Pacific jet (NPJ) stream can support the establishment of a downstream environment that is conducive to EWEs (e.g., Cordeira and Bosart 2010; Bosart et al. 2017). Consequently, the present study addresses the two recommendations from Grotjahn et al. (2016) by adopting an objective NPJ-centered framework to determine the configurations of the NPJ, or NPJ regimes, that are highly conducive to the development of continental U.S. ETEs. The adoption of this framework permits an examination of the degree to which the preferred NPJ configurations prior to ETEs differ depending on both the location of the ETE within the continental U.S. and the meteorological season.

The remainder of this manuscript is structured as follows. Section 2 introduces an identification scheme for continental U.S. ETEs as well as an NPJ Phase Diagram that will be used to characterize the state and evolution of the NPJ prior to the development of ETEs. Section 3 discusses the characteristics of the NPJ prior to the development of continental U.S. ETEs during the cool season employing the NPJ Phase Diagram. Section 4 provides an illustrative example demonstrating how the NPJ Phase Diagram can be applied to examine a synoptic-scale flow evolution that is highly conducive to the development of southern Plains extreme warm events, and section 5 offers a discussion of the results from the previous sections.

2. Methodology

a) ETE identification scheme

This study employs 1-h forecasts of 2-m temperature from the National Centers for Environmental Prediction Climate Forecast System Reanalysis (CFSR; Saha et al. 2010, 2014) during the 36-year period, 1979–2014. The 1-h forecasts of 2-m temperature from the CFSR are 0.5°-resolution and are initialized every 6 h at the standard analysis times (i.e., 0000, 0600, 1200, and 1800 UTC). Given that analyses of 2-m temperature are not available in the CFSR at the standard analysis times, the 1-h forecasts represent a temporally continuous and uniformly gridded dataset of 2-m temperatures that is suitable for identifying continental U.S. ETEs within the CFSR during the period of study. The discussion that follows outlines the ETE identification scheme with respect to continental U.S. extreme warm events.

To identify extreme warm events, 2-m temperature distributions are constructed for each grid point at every forecast verification time during the year (i.e., 4 times daily at 0100, 0700, 1300, and 1900 UTC). A 2-m temperature distribution is constructed for a grid point at a single verification time by isolating the 2-m temperatures for that grid point at 24-h intervals within a 21-day window centered on the verification time for every year between 1979 and 2014. A sample 2-m temperature distribution for the 21-day window centered on 1900 UTC 30 May during 1979–2014 is provided in Fig. 1a for a grid point near Albany, NY.

The 2-m temperature distributions are then leveraged to objectively define thresholds for extreme warmth that are specific to each grid point at a particular verification time. Extreme warm temperatures are defined in the present study as those temperatures that are greater than the 99th-percentile temperature for a grid point at a particular verification time. For the 2-m temperature distribution constructed for a grid point near Albany, NY, the 99th-percentile temperature is 32°C (90°F) at 1900 UTC 30 May (Fig. 1a). A horizontal distribution of the 99th-percentile temperature at 1900 UTC 30 May highlights the considerable spatial variability that characterizes the magnitude of the 99th-percentile temperature over North America (Fig. 1b).

To ensure that the identification scheme captures areas of extreme warmth that are concentrated within the same geographic region, the continental U.S. is split into two domains to the east and west of 105°W[1], respectively (Fig. 1b). For each domain, 1-h forecasts of 2-m temperature that featured at least one grid point over land with a temperature greater than its respective 99th-percentile temperature are catalogued. The catalogued 1-h forecasts within each domain are subsequently ranked according to the number of grid points with temperatures greater than their respective 99th-percentile temperatures. Those 1-h forecasts that rank in the top 5% in terms of the number of grid points featuring extreme warmth are isolated and labeled as extreme warm events within that spatial domain. For example, at least 224 grid points must

---

[1] 105°W is chosen given that it parallels the easternmost extent of the Rocky Mountains, which serve as a natural geographic barrier suitable for partitioning the continental U.S.

exhibit temperatures greater than their respective 99th-percentile temperatures in order for a particular 1-h forecast to qualify as an extreme warm event within the eastern U.S. domain (Fig. 1c). By imposing a minimum gridpoint threshold, the identification scheme ensures that ETEs are extreme not only in terms of their temperatures but also the spatial extent of those extreme temperatures.

Lastly, extreme warm events that occurred within 24 h of another extreme warm event are considered to be the same event and all events are subsequently classified based on the meteorological season (i.e., fall [Sep–Nov], winter [Dec–Feb], spring [Mar–May]) at the time of event initiation. The identification scheme for extreme warm events yields 304 and 264 extreme warm events during 1979–2014 within the eastern and western U.S. domains, respectively (Table 1). A similar methodology is employed to identify continental U.S. extreme cold events by cataloguing 1-h forecasts of 2-m temperature with grid points that featured temperatures less than their respective 1st-percentile temperatures. The identification scheme yields 264 and 269 extreme cold events during 1979–2014 within the eastern and western U.S. domains, respectively (Table 1). As previously mentioned, only ETEs that occurred during the cool season (Sep–May) will be considered in the present study (Table 1). It is left for future work to consider the subset of ETEs that occurred during the summer (Jun–Aug).

Frequency distributions indicating where extreme warm events initiate within the eastern and western U.S. domains during the cool season are shown in Fig. 2, along with the individual event centroids of every extreme warm event at the time of event initiation. The centroid for an individual extreme warm event at the time of event initiation is determined by calculating a weighted average of the latitude and longitude of every grid point that featured a temperature greater than its respective 99th-percentile temperature. Specifically, the latitude and longitude at every qualifying grid point is weighted by the magnitude of the difference between the temperature at the grid point and the 99th-percentile temperature for the grid point. Consequently, an event centroid is focused on those grid points where temperatures exceed their respective 99th-percentile temperatures by the largest margins.

A frequency maximum in eastern U.S. extreme warm event initiation is observed in the northern Plains with a secondary maximum extending from the central and southern Plains eastward towards the southern Mississippi River valley (Fig. 2a). Extreme warm events that impact the U.S. east coast during their lifespan often initiate upstream over the central U.S. before propagating eastward, which may justify a lower frequency of extreme warm event initiation near the U.S. east coast compared to locations farther upstream. In order to investigate whether the NPJ regimes that most frequently precede extreme warm event initiation differ based on the location of ETE initiation within the eastern U.S., *k*-means clustering is used to classify the eastern U.S. extreme warm event centroids into three geographic clusters: the “Northern Plains”, “Southern Plains”, and “East Coast”. The event centroids shown in Fig. 2a are colored based on their respective geographic cluster and match favorably with those locations that feature relative maxima in extreme warm event initiation. The frequency distribution for western U.S. extreme warm event initiation features two primary maxima located in the Pacific Northwest and in the northern U.S. Rocky Mountains, respectively (Fig. 2b), and a secondary maximum in the southwest U.S. As for eastern U.S. extreme warm events, *k*-means clustering is used to classify the western U.S. extreme warm event centroids into three geographic clusters: the “Pacific Northwest”, “Northern Rockies”, and “Southwest”.

Frequency distributions of extreme cold event initiation within the eastern and western U.S. domains during the cool season are shown in Fig. 3. Eastern U.S. extreme cold events most frequently initiate in the northern and southern Plains, with relative maxima also observed in the northeastern Great Lakes region and the middle Mississippi River valley (Fig. 3a). In contrast to eastern U.S. extreme warm events, four geographic clusters were required in order to classify the extreme cold event centroids in a manner consistent with those locations that experience the highest frequency of extreme cold event initiation: the “Northern Plains”, “Northeast”, “Southern Plains”, and “Southeast”. For western U.S. extreme cold event initiation, a frequency maximum is observed in the northern U.S. Rocky Mountains, with a secondary maximum extending along the U.S. west coast and into the southwest U.S. (Fig. 3b). As for western U.S. extreme warm events, the western U.S. extreme cold event centroids are classified into three geographic clusters: the “Pacific Northwest”, “Northern Rockies”, and “Southwest”.

b) The NPJ Phase Diagram

The NPJ regimes that precede continental U.S. ETEs are determined using an NPJ Phase Diagram that is developed from the two leading modes of 250-hPa zonal wind variability during the cool season. The following discussion is nearly identical to that in Winters et al. (2018) and is reproduced here given its relevance to the present study. The NPJ Phase Diagram is developed by employing 250-hPa zonal wind anomalies from the CFSR at every 6-h analysis time during 1979–2014 excluding the summer months. Anomalies are calculated as the deviation of the instantaneous 250-hPa zonal wind from a 21-day running mean centered on each analysis time in order to remove the 36-year mean as well as the annual and diurnal cycles. Specifically, the 21-day running mean at a particular analysis time is calculated from 250-hPa zonal wind data taken at 24-h intervals within a 21-day window centered on the analysis time for every year between 1979 and 2014. A traditional empirical orthogonal function (EOF) analysis (Wilks 2011, Ch. 12) is subsequently performed on the 250-hPa zonal wind anomaly data[2] within a horizontal domain bounded in latitude from 10°N to 80°N and in longitude from 100°E to 120°W in order to capture the upper-tropospheric flow pattern over the North Pacific basin and to determine the two leading modes of NPJ variability.

The regression of 250-hPa zonal wind anomaly data onto the first two standardized principal components, PC 1 and PC 2, obtained from the traditional EOF analysis reveals the spatial structures of EOF 1 and EOF 2, respectively (Fig. 4). EOF 1 explains 10.3% of the variance of 250-hPa zonal wind over the North Pacific during the cool season and corresponds to longitudinal variability of 250-hPa zonal wind in the vicinity of the exit region of the climatological NPJ. A positive EOF 1 pattern (+EOF 1) is associated with a zonal extension of the exit region of the climatological NPJ (i.e., a jet extension), while a negative EOF 1 pattern (–EOF 1) is associated with a retraction of the exit region of the climatological NPJ (i.e., a jet retraction). EOF 2 explains 7.8% of the variance of 250-hPa zonal wind over the North Pacific during the cool season and corresponds to latitudinal variability of 250-hPa zonal wind in the vicinity of the exit region of the climatological NPJ. A positive EOF 2 pattern (+EOF 2) is associated with a poleward shift of the exit region of the climatological NPJ (i.e., a poleward shift), while a negative EOF 2 pattern (–EOF 2) is associated with an equatorward shift of the exit region of the climatological NPJ (i.e., an equatorward shift).

The EOF patterns and the combined variance explained by EOF 1 and EOF 2 are comparable to that found in previous studies of NPJ variability (Athanasiadis et al. 2010; Jaffe et al. 2011; Griffin and Martin 2017) and the two leading EOFs are statistically well separated using the methodology outlined in North et al. (1982). Furthermore, the combined variance

---

[2] 250-hPa zonal wind anomalies are weighted by the square root of the cosine of latitude prior to the application of traditional EOF analysis.

explained by EOF 1 and EOF 2 is comparable to the variance explained by well-established atmospheric teleconnection patterns such as the Madden–Julian Oscillation (Wheeler and Hendon 2004), the Pacific–North American pattern (Barnston and Livesey 1987), the Arctic Oscillation (Thompson and Wallace 1998), and the North Atlantic Oscillation (Barnston and Livesey 1987).

The magnitude and sign of PC 1 and PC 2 are normalized to unit variance and provide an indication of how strongly the instantaneous 250-hPa zonal wind anomalies project onto EOF 1 and EOF 2, respectively. Time series constructed from the instantaneous PCs subsequently assist in characterizing the temporal evolution of the NPJ with respect to EOF 1 and EOF 2. The use of instantaneous PCs produces a noisy time series, however, due to the high-frequency variability that characterizes the NPJ on daily time scales (e.g., Griffin and Martin 2017; their Fig. 1). Consequently, in an attempt to describe the evolution of the NPJ with greater temporal coherence than the instantaneous PCs while preserving the high-frequency variability of the NPJ on daily time scales, the instantaneous PCs are smoothed through the calculation of a weighted average of the instantaneous PCs within ±24 h of each analysis time, t_0. The weight, w, prescribed to the instantaneous PCs at each analysis time, t, within ±24 h of t_0 is defined as: $w = 5 – |t– t_0|/6$, for $|t – t_0| \leq 24$ h.

The weighted PCs at a particular analysis time can then be plotted on a two-dimensional Cartesian grid (i.e., the NPJ Phase Diagram) in an effort to visualize the state of the NPJ and to define the prevailing NPJ regime (Fig. 5). The position along the abscissa (ordinate) within the NPJ Phase Diagram corresponds to the value of weighted PC 1 (PC 2) and indicates how strongly the 250-hPa zonal wind anomalies project onto EOF 1 (EOF 2). It is important to note that the upper-tropospheric flow pattern over the North Pacific is characterized by considerable variability, such that the flow pattern at any particular time is more complex than that suggested by the NPJ Phase Diagram. Nevertheless, given that the NPJ Phase Diagram captures the two leading modes of 250-hPa zonal wind variability over the North Pacific, plotting the weighted PCs in the NPJ Phase Diagram and tracking their evolution over time captures many important features of the NPJ evolution.

As demonstrated extensively in prior work, each NPJ regime exhibits a strong influence on the character of the downstream large-scale flow pattern over North America (e.g., Athanasiadis et al. 2010; Jaffe et al. 2011; Griffin and Martin 2017; Winters et al. 2018). To highlight this influence, the weighted PCs are calculated for all analysis times in the CFSR during 1979–2014 excluding the summer months and are subsequently classified into NPJ regimes according to Fig. 5. Periods during which the NPJ is a Euclidean distance of at least 1 PC unit from the origin of the NPJ Phase Diagram and characterized by the same NPJ regime for at least three consecutive days are isolated for composite analysis. Composite analyses of the upper- (Fig. 6) and lower-tropospheric (Fig. 7) flow patterns 4 days following the initiation of each NPJ regime effectively describe the the relationship between each NPJ regime and lower-tropospheric temperatures over North America.

A jet extension features a strong, zonally-oriented NPJ that extends towards the U.S. west coast (Fig. 6a) and is associated with above- and below-normal temperatures over western and eastern North America, respectively (Fig. 7a). A jet retraction is characterized by an anomalous upper-tropospheric ridge over the central North Pacific that results in a retracted NPJ over the western North Pacific and a split NPJ to the east of the dateline (Fig. 6b). Jet retractions are also associated with below-normal temperatures along the west coast of North America and above-normal temperatures in parts of the southern Plains and Ohio River valley (Fig. 7b). A poleward shift is characterized by a strong NPJ whose exit region is deflected poleward towards the Pacific Northwest (Fig. 6c), as well as above-normal temperatures across northern North America (Fig. 7c). Lastly, an equatorward shift is associated with an anomalous upper-tropospheric ridge over the high-latitude North Pacific and an anomalous trough over the subtropical North Pacific, reminiscent of a Rex block (Rex 1950), that results in an equatorward deflection of the NPJ (Fig. 6d). Below-normal temperatures are also observed across northern North America in conjunction with an equatorward shift (Fig. 7d).

Considered together, the composite analyses suggest that parts of North America may be more susceptible to the development of an ETE based on the prevailing NPJ regime. To evaluate the veracity of this suggestion, the prevailing NPJ regime prior to each continental U.S. ETE is determined by calculating the weighted PCs at 6-h intervals during the 3–7-day period prior to ETE initiation[3]. The weighted PCs are then averaged to determine the mean position of the NPJ within the NPJ Phase Diagram 3–7 days prior ETE initiation (i.e., ETE PC 1, and ETE PC 2). Lastly, every ETE is classified into an NPJ regime based on the magnitude and sign of ETE PC 1 and ETE PC 2 according to Fig. 5.

3. NPJ regimes and evolutions that precede cool season ETEs

a) Extreme warm events

Histograms illustrating the frequency with which eastern U.S. (Fig. 8a) and western U.S. (Fig. 9a) extreme warm events initiate following each NPJ regime highlight the considerable variability that characterizes the upper-tropospheric flow pattern over the North Pacific prior to ETE initiation. Overall, eastern U.S. extreme warm events (N=239) are more common during the fall (N=86) and winter (N=84) compared to the spring (N=69), and most frequently initiate

---

[3] The time of ETE initiation is rounded to the nearest analysis time for the present study.

following jet retractions (N=69) and poleward shifts (N=66) throughout the cool season (Fig. 8a). This result is consistent with the observation that jet retractions and poleward shifts are generally associated with upper-tropospheric ridges (Figs. 6b,c) and above-normal temperatures (Figs. 7b,c) over parts of eastern North America. The most frequent NPJ regime prior to eastern U.S. extreme warm event initiation varies based on the meteorological season, however. Specifically, eastern U.S. extreme warm events most frequently initiate following equatorward shifts (N=26) during the fall, following jet retractions (N=27) during the winter, and following both jet retractions (N=20) and poleward shifts (N=20) during the spring.

The characteristics of eastern U.S. extreme warm events also vary between the three eastern U.S. geographic clusters. Northern Plains extreme warm events (N=94) are most common during the winter (N=40) and are preceded by jet extensions (N=18) with the lowest frequency throughout the cool season (Fig. 8b). However, those Northern Plains extreme warm events that occur during the winter are nearly as frequent following jet extensions (N=12) as they are following jet retractions (N=11) and poleward shifts (N=10). Similar to Northern Plains extreme warm events, Southern Plains extreme warm events (N=84) are also more common during the winter (N=33) compared to fall (N=26) and spring (N=25) (Fig. 8c). Southern Plains extreme warm events most frequently initiate following jet retractions (N=35) throughout the cool season and do not exhibit any seasonal variability with respect to the most frequent NPJ regime prior to event initiation. In contrast to Northern Plains and Southern Plains extreme warm events, East Coast extreme warm events (N=61) are more common during the fall (N=31) than during the spring (N=19) and winter (N=11) (Fig. 8d). East Coast extreme warm events most frequently initiate following poleward shifts (N=20) throughout the cool season, though the most frequent NPJ regime prior to event initiation depends on the meteorological season.

Western U.S. extreme warm events (N=204) are most common during the winter (N=81) and are preceded by jet retractions (N=41) with the lowest frequency throughout the cool season (Fig. 9a). This result is consistent with the observation that jet retractions are generally associated with an anomalous upper-tropospheric trough (Fig. 6b) and below-normal temperatures (Fig. 7b) over the western U.S. Similar to eastern U.S. extreme warm events, the most frequent NPJ regimes that precede the initiation of western U.S. extreme warm events depend on the meteorological season. Specifically, western U.S. extreme warm events most frequently initiate following poleward shifts (N=23) and jet retractions (N=19) during the fall, following jet extensions (N=32) and equatorward shifts (N=25) during the winter, and following equatorward shifts (N=20) and poleward shifts (N=18) during the spring.

Consideration of events within each of the three western U.S. geographic clusters adds further insight into the characteristics of western U.S. extreme warm events. Pacific Northwest extreme warm events (N=89) are most common during the winter (N=37), and most frequently initiate following jet extensions (N=27) and equatorward shifts (N=27) throughout the cool season (Fig. 9b). As observed for all western U.S. extreme warm events, however, the most frequent NPJ regimes prior to Pacific Northwest extreme warm events vary based on the meteorological season. Specifically, Pacific Northwest extreme warm events most frequently initiate following poleward shifts (N=11) and jet retractions (N=7) during the fall, and following jet extensions and equatorward shifts during the winter (N=16 and N=13, respectively) and spring (N=8 and N=10, respectively) (Fig. 9b). The most frequent NPJ regime prior to Northern Rockies extreme warm events is also characterized by considerable seasonal variability (Fig. 9c). However, in contrast to Pacific Northwest extreme warm events, Northern Rockies extreme warm events (N=46) initiate following equatorward shifts (N=7) with the lowest frequency throughout the cool season. Southwest extreme warm events (N=69) initiate most frequently following equatorward shifts (N=20) and poleward shifts (N=19) throughout the cool season (Fig. 9d), though the most frequent NPJ regime prior to event initiation differs based on the meteorological season as observed for the other western U.S. geographic clusters.

The construction of composite trajectories of the NPJ within the NPJ Phase Diagram provides an objective characterization of the evolution of the NPJ during the 10-day period prior to ETE initiation. Composite trajectories of the NPJ within the NPJ Phase Diagram are constructed by calculating the weighted PCs at 6-h intervals during the 10-day period prior to the initiation of every ETE. The weighted PCs prior to each ETE are then shifted so that the position of the NPJ always lies at the origin of the NPJ Phase Diagram 10 days prior to ETE initiation. Lastly, the weighted PCs that correspond to the same lead time prior to ETE initiation are averaged among all ETEs within the same geographic cluster to construct a composite trajectory of the NPJ within the NPJ Phase Diagram.

The composite trajectories of the NPJ within the NPJ Phase Diagram prior to all eastern U.S. extreme warm events and prior to extreme warm events within the three eastern U.S. geographic clusters are shown in Fig. 10a. Consistent with the observation that eastern U.S. extreme warm events most frequently initiate following jet retractions and poleward shifts throughout the cool season (Fig. 8a), the composite trajectory for all eastern U.S. extreme warm events indicates that the NPJ evolves towards a jet retraction and poleward shift during the 10-day period prior to event initiation. A similar trajectory is generally found for extreme warm events within each of the eastern U.S. geographic clusters as well, with Northern Plains extreme warm events characterized by an NPJ that evolves predominantly towards a poleward shift, and Southern Plains and East Coast extreme warm events characterized by an NPJ that evolves predominantly towards a jet retraction.

The composite trajectory prior to all western U.S. extreme warm events differs considerably compared to the trajectory for eastern U.S. extreme warm events (Fig. 10b). In particular, the composite trajectory for all western U.S. extreme warm events indicates that the NPJ evolves towards a jet extension and equatorward shift during the 10-day period prior to event initiation, rather than the jet retraction and poleward shift observed for all eastern U.S. events (Fig. 10a). Consequently, the evolution of the NPJ within the NPJ Phase Diagram provides an indication as to whether the large-scale flow pattern is generally more conducive to the development of an extreme warm event in the eastern or western U.S. The trajectories associated with the three western U.S. geographic clusters are characterized by notable differences, however. Specifically, Pacific Northwest extreme warm events are characterized by an NPJ that evolves towards a jet extension, while Southwest extreme warm events are characterized by an NPJ that evolves towards an equatorward shift and jet retraction during the 10-day period prior to event initiation. In contrast to Pacific Northwest and Southwest extreme warm events, the trajectory for Northern Rockies events does not deviate far from the origin of the NPJ Phase Diagram. Consequently, Northern Rockies extreme warm events do not appear to have a preferred NPJ evolution prior to event initiation.

b) Extreme cold events

The variability in NPJ regimes that precede the initiation of continental U.S. extreme cold events is also examined in the context of the NPJ Phase Diagram. Figure 11a indicates that eastern U.S. extreme cold events (N=173) are more common during the winter (N=63) and spring (N=60) compared to the fall (N=50), and more frequently initiate following equatorward shifts (N=73) compared to the other NPJ regimes by a large margin throughout the cool season.

This result is consistent with the observation that equatorward shifts are generally associated with an anomalous upper-tropospheric trough (Fig. 6d) and below-normal temperatures (Fig. 7d) across northern North America. As observed for eastern U.S. extreme warm events, the most frequent NPJ regime prior to eastern U.S. extreme cold events depends on the meteorological season. In particular, eastern U.S. extreme cold events most frequently initiate following equatorward shifts (N=17) and jet extensions (N=17) during the fall, and following only equatorward shifts during the winter (N=30) and spring (N=26).

The same characteristics derived for all eastern U.S. extreme cold events generally apply to each of the four eastern U.S. geographic clusters, as well. Specifically, extreme cold events within each geographic cluster are most common during the winter or spring, and most frequently initiate following equatorward shifts throughout the cool season (Figs. 11b–e). The lack of any considerable differences in extreme cold event characteristics between the four eastern U.S. geographic clusters stands in contrast to the considerable differences observed between geographic clusters for eastern U.S. extreme warm events (Figs. 8a–d). Consequently, this result implies that there is larger variability among the upper-tropospheric flow patterns that are conducive to the development of eastern U.S. extreme warm events than among those that are conducive to eastern U.S. extreme cold events.

In contrast to western U.S. extreme warm events (Fig. 9a), western U.S. extreme cold events (N=196) are the least common during the winter (N=52) and are most common during the spring (N=83) (Fig. 12a). Similar seasonal distributions of extreme cold events are also observed for the three western U.S. geographic clusters (Figs. 12b–d). Additionally, western U.S. extreme cold events most frequently initiate following jet retractions (N=59) throughout the cool season (Fig. 12a), rather than with the lowest frequency (N=41) as observed for western U.S. extreme warm events (Fig. 9a). This result is consistent with the observation that jet retractions are generally associated with an anomalous upper-tropospheric trough (Fig. 6b) and below-normal temperatures (Fig. 7b) along the U.S. west coast. As observed for eastern U.S. extreme cold events, the most frequent NPJ regime prior to the initiation of western U.S. extreme cold events varies based on meteorological season. Specifically, western U.S. extreme cold events most frequently initiate following equatorward shifts (N=21) and jet extensions (N=18) during the fall, and following jet retractions during the winter (N=21) and spring (N=28).

The NPJ regimes that most frequently precede extreme cold event initiation throughout the cool season differ among the western U.S. geographic clusters, unlike the eastern U.S. geographic clusters. Pacific Northwest extreme cold events (N=78) most frequently initiate following jet retractions (N=31) throughout the cool season (Fig. 12b), with most of those events occurring during the winter (N=11) and spring (N=15). During the fall, however, Pacific Northwest extreme cold events initiate following equatorward shifts (N=12) more frequently than the other three NPJ regimes. Northern Rockies extreme cold events (N=55), on the other hand, most frequently initiate following equatorward shifts (N=22) throughout the cool season (Fig. 12c), while Southwest extreme cold events (N=63) initiate following equatorward shifts (N=10) with the *lowest* frequency throughout the cool season (Fig. 12d). The most frequent NPJ regime prior to the initiation of Southwest extreme cold events depends on the meteorological season, with events most frequently initiating following jet extensions during the fall (N=8), following jet retractions during the winter (N=6), and nearly equivalently following jet extensions (N=9), jet retractions (N=8), and poleward shifts (N=8) during the spring.

In contrast to the composite trajectories for eastern and western U.S. extreme warm events (Figs. 10a,b), the composite trajectories for eastern and western U.S. extreme cold events are rather similar (Figs. 13a,b). In particular, the composite trajectories for eastern and western U.S. extreme cold events both indicate that the NPJ evolves towards an equatorward shift and slight jet extension during the 10-day period prior to event initiation (Figs. 13a,b). Therefore, unlike for extreme warm events, knowledge of the evolution of the NPJ within the NPJ Phase Diagram is not enough on its own to suggest whether the eastern or western U.S. is more susceptible to extreme cold event initiation.

Differences in the evolution of the NPJ within the NPJ Phase Diagram are observed between the geographic clusters, however. Similar to the trajectory for all eastern U.S. extreme cold events, the composite trajectories prior to the initiation of Northern Plains, Southern Plains, and Southeast extreme cold events suggest that the NPJ generally evolves towards an equatorward shift during the 10-day period prior to event initiation (Fig. 13a). The composite trajectory prior to the initiation of Northeast extreme cold events differs from the other eastern U.S. clusters, however, with the NPJ evolving towards a jet extension during the 10-day period prior to event initiation. The Pacific Northwest and Northern Rockies trajectories are comparable to the trajectory for all western U.S. extreme cold events in that they both show the NPJ evolving towards an equatorward shift and jet extension by the time of extreme cold event initiation (Fig. 13b). The Southwest trajectory also suggests that the NPJ evolves towards an equatorward shift, but the trajectory differs from the Pacific Northwest and Northern Rockies trajectories given that the NPJ evolves towards a slight jet retraction by the time of extreme cold event initiation rather than a jet extension.

4. Composite evolution of Southern Plains extreme warm events preceded by a jet retraction

The preceding analyses demonstrate that the most frequent NPJ regimes and NPJ evolution prior to continental U.S. ETEs during the cool season vary considerably based on the location of ETE initiation. Provided with this result, the NPJ Phase Diagram can be applied to isolate ETEs within a particular geographic region that initiate following the same NPJ regime. A composite analysis can subsequently be performed on the isolated ETEs to determine the synoptic-dynamic mechanisms that permit the flow to evolve from an antecedent NPJ regime to ETE initiation within a particular geographic region. The forthcoming discussion provides an illustrative example that showcases the utility of such an analysis by investigating the synoptic-scale flow evolution most conducive to Southern Plains extreme warm events. The Southern Plains cluster is selected for analysis given that it is the only geographic region where the most frequent NPJ regime prior to both extreme warm and cold events does not vary based on the meteorological season (Figs. 8, 9, 11 and 12). Furthermore, extreme warm events during the cool season are selected due to the limited consideration those events have received in the refereed literature compared to extreme cold events.

A composite analysis of the synoptic-scale flow evolution found to be most conducive to the initiation of Southern Plains extreme warm events during the cool season is performed by isolating those Southern Plains extreme warm events that are characterized by a jet retraction prior to event initiation (N=35; Fig. 8c). The latitude and longitude of the individual Southern Plains event centroids (Fig. 2a) are then averaged to determine the position of a composite centroid. The composite analyses are constructed by, first, shifting the CFSR data for each individual event so that each individual event centroid matches the position of the composite centroid and, second, by averaging the shifted CFSR data at each grid point across all cases within the horizontal domain shown in Fig. 14. A two-sided Student's *t* test is performed on the composite 250-hPa geopotential height anomalies and 850-hPa temperature anomalies to identify regions that are statistically significantly different from climatology at the 99% confidence level.

The composite evolution of the synoptic-scale flow pattern during the 6-day period prior to event initiation is provided in Fig. 14 and is comparable to the evolution of southeast U.S. extreme warm events that develop during a negative phase of the PNA discussed by Westby and Black (2015). An anomalous upper-tropospheric ridge is located over the central North Pacific 6 days prior to event initiation, resulting in a jet retraction over the western North Pacific and a split NPJ to the east of the dateline (Fig. 14a). Farther downstream, an anomalous upper-tropospheric ridge is collocated with above-normal 850-hPa temperatures over the southern Plains and northern Mexico (Fig. 14b), suggesting that the synoptic-scale environment may be preconditioned for the development of extreme warmth in that location.

4 days prior to event initiation, the anomalous North Pacific ridge amplifies further compared to the prior time in conjunction with surface cyclogenesis beneath the left-exit region of the retracted NPJ (Figs. 14c,d). Specifically, the surface cyclone facilitates anomalous warm-air advection over the central North Pacific that contributes to both upper-tropospheric height rises and forcing for quasigeostrophic ascent (not shown). The presence of anomalous precipitable water in the central North Pacific also suggests that condensational heating is likely associated with any areas of ascent and, consequently, that diabatic processes contribute to the observed ridge amplification (e.g., Massacand et al. 2001; Riemer et al. 2008; Torn 2010; Grams et al. 2011; Madonna et al. 2014; Pfahl et al. 2015; Torn and Hakim 2015; Grams and Archambault 2016; Bosart et al. 2017). Central North Pacific ridge amplification subsequently results in the amplification of the downstream upper-tropospheric flow pattern 2 days prior to event initiation (Fig. 14e), including the development of a positively-tilted trough along the west

coast of North America and additional ridge amplification over the southern Plains. The amplified upper-tropospheric flow pattern also supports lee cyclogenesis over the northern U.S. Rocky Mountains and surface anticyclogenesis over the southeast U.S. (Fig. 14f). The intensified pressure gradient between the lee cyclone and surface anticyclone induces southwesterly geostrophic flow over central North America and the concomitant advection of anomalous warmth from northern Mexico into the southern Plains.

The lee cyclone intensifies further by the time of event initiation beneath the entrance region of a 250-hPa jet streak and in conjunction with continued amplification of the upper-tropospheric flow pattern (Figs. 14g,h). The intensified lee cyclone subsequently facilitates stronger southwesterly geostrophic flow over the southern Plains than at the prior time, which ensures that the advection of anomalous warmth into the southern Plains continues unabated until the time of event initiation. Notably, the composite evolution also features anomalous precipitable water over the middle Mississippi River valley at the time of event initiation (Fig. 14g). Given the strong dynamical forcing for ascent provided by the amplified upper-tropospheric flow pattern and the presence of the lee cyclone, the evolution of a Southern Plains extreme warm event bears a strong resemblance to synoptic-scale flow evolutions that are conducive to the development of eastern U.S. extreme precipitation events during the cool season (e.g., Moore et al. 2015; Moore 2017). Consequently, it is possible that extreme precipitation events may accompany the development of Southern Plains extreme warm events on occasion.

5. Discussion

The utility of the NPJ Phase Diagram is that it provides a common framework for examining the antecedent synoptic-scale flow patterns associated with ETEs regardless of the location of the ETE within the continental U.S. Overall, eastern U.S. extreme warm events are most frequent following jet retractions and poleward shifts and are characterized by an NPJ that evolves towards those same two NPJ regimes within the NPJ Phase Diagram during the 10-day period prior to ETE initiation. Western U.S. extreme warm events, however, are the *least* frequent following jet retractions and are characterized by an NPJ that evolves towards a jet extension and equatorward shift within the NPJ Phase Diagram during the 10-day period prior to ETE initiation. Eastern U.S. extreme cold events are more frequent following equatorward shifts compared to the other NPJ regimes by a large margin, while western U.S. extreme cold events are most frequent following both jet retractions and equatorward shifts. Furthermore, both eastern and western U.S. extreme cold events are generally characterized by an evolution of the NPJ towards an equatorward shift during the 10-day period prior to ETE initiation. Considered together, the analysis suggests that knowledge of both the prevailing NPJ regime and the NPJ evolution can provide an indication of the degree to which the synoptic-scale flow pattern may be conducive to ETE initiation within certain parts of the continental U.S.

While the NPJ regimes and NPJ evolutions described above are those that most frequently characterize all eastern and western U.S. ETEs throughout the cool season, the most frequent NPJ regime prior to ETE initiation varies considerably based on the specific location of ETE initiation within the eastern and western U.S. domains as well as based on the meteorological season. As an example, Pacific Northwest extreme cold events most frequently initiate following jet retractions throughout the cool season, while Northern Rockies extreme cold events initiate following jet retractions with the *lowest* frequency throughout the cool season. Additionally, Pacific Northwest extreme cold events most frequently initiate following jet retractions only during the winter and spring. During the fall, Pacific Northwest events most frequently initiate following equatorward shifts. The considerable spatial variability that characterizes the most frequent NPJ regime prior to ETE initiation motivates future studies to focus on the types of synoptic-scale flow patterns that facilitate ETE initiation with specific geographic regions, similar to the approaches of Westby and Black (2015), Grotjahn et al. (2017), and Xie et al. (2017).

The NPJ Phase Diagram and the results from the present study provide a starting point for detailed investigations into the types of synoptic-scale flow patterns that facilitate ETE initiation within a specific geographic region. As an illustrative example, the analysis in section 4 employs the NPJ Phase Diagram to investigate the synoptic-scale flow evolution that is most conducive to the initiation of Southern Plains extreme warm events. In geographic clusters where multiple NPJ regimes are frequently observed prior to ETE initiation (e.g., Pacific Northwest extreme cold events), the NPJ Phase Diagram can be applied to isolate ETEs that are preceded by the same NPJ regime. Composite analyses can then be performed on events that are preceded by the same NPJ regime in order to examine the differences between a set of synoptic-scale flow evolutions that are mutually conducive to ETE initiation and to identify the characteristic origins of anomalously warm and cold air masses during the selected events. Such examinations represent promising areas of future work.

The capability of the NPJ Phase Diagram to identify NPJ regimes and NPJ evolutions that are conducive to the development of ETEs highlights the potential for the NPJ Phase Diagram to add value to operational medium-range (6–10 day) forecasts of temperature over the continental U.S. In particular, the NPJ Phase Diagram can be employed operationally to determine both the prevailing NPJ regime and the forecast evolution of the NPJ. This information can be paired with the results of this study to determine the geographic locations that may be more susceptible to the development of anomalous temperatures during the medium-range period. Despite this potential, however, additional studies that utilize the NPJ Phase Diagram are required in order to differentiate between NPJ evolutions within the NPJ Phase Diagram that are conducive to ETEs and those that result in nonextreme events. Additionally, Winters et al. (2018) indicate that certain NPJ regimes are generally characterized by enhanced or reduced forecast skill during the medium-range forecast period. Additional studies that examine the medium-range forecast skill of ETEs with respect to the NPJ Phase Diagram might reveal whether certain synoptic-scale flow evolutions prior to ETEs are characterized by enhanced or reduced forecast skill.

Lastly, the NPJ Phase Diagram can be applied to examine the variability in NPJ regimes that precede other types of North American EWEs during the cool season. For instance, the NPJ Phase Diagram can be applied to determine the NPJ regimes that are conducive to the development of extreme precipitation events (e.g., Moore et al. 2015; Moore 2017), landfalling atmospheric river events (e.g., Zhu and Newell 1998; Ralph et al. 2004; Neiman et al. 2008; Cordeira et al. 2013; Mundhenk et al. 2016; Gershunov et al. 2017), severe weather outbreaks (e.g., Cook and Schaefer 2008; Allen et al. 2015; Tippett et al. 2015; Gensini and Marinaro 2016; Cook et al. 2017), and rapidly-deepening midlatitude cyclones (e.g., Sanders and Gyakum 1980; Bosart et al. 1996; Isard et al. 2000; Grise et al. 2013; Bentley 2018). As demonstrated for ETEs, these examinations have the potential to add value to operational forecasts of EWEs through further understanding of the environments that are conducive to EWE development.

Acknowledgments

The authors thank Mike Bodner, Daniel Halperin, Arlene Laing, Bill Lamberson, Sara Ganetis, and Josh Kastman for their constructive discussions concerning the NPJ Phase Diagram. The authors also thank the National Oceanic and Atmospheric Administration for its support of this work via Grant NA15NWS4680006.

References

Allen, J. T., M. K. Tippett, and A. H. Sobel, 2015: Influence of the El Niño/Southern Oscillation on tornado and hail frequency in the United States. *Nat. Geosci.*, **8,** 278–283, doi: 10.1038/ngeo2385.

Athanasiadis, P. J., J. M. Wallace, and J. J. Wettstein, 2010: Patterns of wintertime jet stream variability and their relation to the storm tracks. *J. Atmos. Sci.*, **67**, 1361–1381, doi: 10.1175/2009JAS3270.1.

Barnston, A. G., and R. E. Livesey, 1987: Classification, seasonality, and persistence of low-frequency atmospheric circulation patterns. *Mon. Wea. Rev.*, **115**, 1083–1126, doi: 10.1175/1520-0493(1987)115<1083:CSAPOL>2.0.CO;2.

Bell, G. D., and L. F. Bosart, 1988: Appalachian cold-air damming. *Mon. Wea. Rev.*, **116,** 137–161, doi: 10.1175/1520-0493(1988)116<0137:ACAD>2.0.CO;2.

Bentley, A. M., 2018: Extratropical cyclones leading to extreme weather events over central and eastern North America. Ph.D. Dissertation, University at Albany, SUNY, 158 pp.

Bosart, L. F., G. J. Hakim, K. R. Tyle, M. A. Bedrick, W. E. Bracken, M. J. Dickinson, and D. M. Schultz, 1996: Large-scale antecedent conditions associated with the 12–14 March 1993 cyclone ("Superstorm '93") over eastern North America. *Mon. Wea. Rev.*, **124,** 1865–1891, doi: 10.1175/1520-0493(1996)124<1865:LSACAW>2.0.CO;2.

Bosart, L. F., B. J. Moore, J. M. Cordeira, and H. M. Archambault, 2017: Interactions of North Pacific tropical, midlatitude, and polar disturbances resulting in linked extreme weather events over North America in October 2007. *Mon. Wea. Rev.*, **145,** 1245–1273, doi: 10.1175/MWR-D-16-0230.1.

Brewer, M. C., C. F. Mass, and B. E. Potter, 2012: The west coast thermal trough: Climatology and synoptic evolution. *Mon. Wea. Rev.*, **140,** 3820–3843, doi: 10.1175/MWR-D-12-00078.1.

Brewer, M. C., C. F. Mass, and B. E. Potter, 2013: The west coast thermal trough: Mesoscale evolution and sensitivity to terrain and surface fluxes. *Mon. Wea. Rev.*, **141,** 2869–2896, doi: 10.1175/MWR-D-12-00305.1.

Carrera, M. L., R. W. Higgins, and V. E. Kousky, 2004: Downstream weather impacts associated with atmospheric blocking over the northeast Pacific. *J. Climate*, **17,** 4823–4839, doi: 10.1175/JCLI-3237.1.

Cellitti, M. P., J. E. Walsh, R. M. Rauber, and D. H. Portis, 2016: Extreme cold air outbreaks over the United States, the polar vortex, and the large-scale circulation. *J. Geophys. Res.*, **111,** D02114, doi: 10.1029/2005JD006273.

Colle, B. A., and C. F. Mass, 1995: The structure and evolution of cold surges east of the Rocky Mountains. *Mon. Wea. Rev.*, **123,** 2577–2610, doi: 10.1175/1520-0493(1995)123<2577:TSAEOC>2.0.CO;2.

Colucci, S. J., and J. C. Davenport, 1987: Rapid surface anticyclogenesis: Synoptic climatology and attendant large-scale circulation changes. *Mon. Wea. Rev.*, **115,** 822–836, doi: 10.1175/1520-0493(1987)115<0822:RSASCA>2.0.CO;2.

Cook, A. R., and J. T. Schaefer, 2008: The relation of El Niño–Southern Oscillation (ENSO) to winter tornado outbreaks. *Mon. Wea. Rev.*, **136,** 3121–3137, doi: 10.1175/2007MWR2171.1.

Cook, A. R., L. M. Leslie, D. B. Parsons, and J. T. Schaefer, 2017: The impact of El Niño–Southern Oscillation (ENSO) on winter and early spring U.S. tornado outbreaks. *J. Appl. Meteor. Climatol.*, **56,** 2455–2478, doi: 10.1175/JAMC-D-16-0249.1.

Cordeira, J. M., and L. F. Bosart, 2010: The antecedent large-scale conditions of the "Perfect Storms" of late October and early November 1991. *Mon. Wea. Rev.*, **138,** 2546–2569, doi: 10.1175/2010MWR3280.1.

Cordeira, J. M., F. M. Ralph, and B. J. Moore, 2013: The development and evolution of two atmospheric rivers in proximity to western North Pacific tropical cyclones in October 2010. *Mon. Wea. Rev.*, **141,** 4234–4255, doi: 10.1175/MWR-D-13-00019.1.

Dallavalle, J. P., and L. F. Bosart, 1975: A synoptic investigation of anticyclogenesis accompanying North American polar air outbreaks. *Mon. Wea. Rev.*, **103,** 941–957, doi: 10.1175/1520-0493(1975)103<0941:ASIOAA>2.0.CO;2.

Dole, R., M. Hoerling, A. Kumar, J. Eischeid, J. Perlwitz, X.-W. Quan, G. Kiladis, R. Webb, D. Murray, M. Chen, K. Wolter, and T. Zhang, 2014: The making of an extreme event: Putting the pieces together. *Bull. Amer. Meteor. Soc.*, **95,** 427–440, doi: 10.1175/BAMS-D-12-00069.1.

Downton, M. W., and K. A. Miller, 1993: The freeze risk to Florida citrus. Part II: Temperature variability and circulation patterns. *J. Climate*, **6,** 364–372, doi: 10.1175/1520-0442(1993)006<0364:TFRTFC>2.0.CO;2.

Gensini, V. A., and A. Marinaro, 2016: Tornado frequency in the United States related to global relative angular momentum. *Mon. Wea. Rev.*, **144,** 801–810, doi: 10.1175/MWR-D-15-0289.1.

Gershunov, A., T. Shulgina, F. M. Ralph, D. A. Lavers, and J. J. Rutz, 2017: Assessing the climate-scale variability of atmospheric rivers affecting western North America. *Geophys. Res. Lett.*, **44,** 7900–7908, doi: 10.1002/2017GL074175.

Grams, C. M., and Coauthors, 2011: The key role of diabatic processes in modifying the upper-tropospheric wave guide: A North Atlantic case-study. *Quart. J. Roy. Meteor. Soc.*, **137,** 2174–2193, doi: 10.1002/qj.891.

Grams, C. M., and H. M. Archambault, 2016: The key role of diabatic outflow in amplifying the midlatitude flow: A representative case study of weather systems surrounding western North Pacific extratropical transition. *Mon. Wea. Rev.*, **144**, 3847–3869, doi: 10.1175/MWR-D-15-0419.1.

Griffin, K. S., and J. E. Martin, 2017: Synoptic features associated with temporally coherent modes of variability of the North Pacific jet stream. *J. Climate*, **30**, 39–54, doi: 10.1175/JCLI-D-15-0833.1.

Grise, K. M., S.-W. Son, J. R. Gyakum, 2013: Intraseasonal and interannual variability in North American storm tracks and its relationship to equatorial Pacific variability. *Mon. Wea. Rev.*, **141,** 3610–3625, doi: 10.1175/MWR-D-12-00322.1.

Grotjahn, R., and Coauthors, 2016: North American extreme temperature events and related large scale meteorological patterns: A review of statistical methods, dynamics, modeling, and trends. *Climate Dyn.*, **46,** 1151–1184, doi: 10.1007/s00382-015-2638-6.

Grotjahn, R., and R. Zhang, 2017: Synoptic analysis of cold air outbreaks over the California Central Valley. *J. Climate*, **30,** 9417–9433, doi: 10.1175/JCLI-D-17-0167.1.

Gu, L., P. J. Hanson, W. Mac Post, D. P. Kaiser, B. Yang, R. Nemani, S. G. Pallardy, and T. Meyers, 2008: The 2007 eastern US spring freeze: Increased cold damage in a warming world? *Bioscience*, **58,** 253–262, doi: 10.1641/B580311.

Guirguis, K., A. Gershunov, R. Schwartz, and S. Bennett, 2011: Recent warm and cold daily winter temperature extremes in the Northern Hemisphere. *Geophys. Res. Lett.*, **38,** L17701, doi: 10.1029/2011GL048762.

Hartjenstein, G., and R. Bleck, 1991: Factors affecting cold-air outbreaks east of the Rocky Mountains. *Mon. Wea. Rev.*, **119,** 2280–2292, doi: 10.1175/1520-0493(1991)119<2280:FACAOE>2.0.CO;2.

Hartmann, D. L., 2015: Pacific sea surface temperature and the winter of 2014. *Geophys. Res. Lett.*, **42,** 1894–1902, doi: 10.1002/2015GL063083.

Higgins, R. W., A. Leetmaa, and V. E. Kousky, 2002: Relationships between climate variability and winter temperature extremes in the United States. *J. Climate*, **15,** 1555–1572, doi: 10.1175/1520-0442(2002)015<1555:RBCVAW>2.0.CO;2.

Hoerling, M., A. Kumar, R. Dole, J. W. Nielsen-Gammon, J. Eischeid, J. Perlwitz, X.-W. Quan, T. Zhang, P. Pegion, and M. Chen, 2013: Anatomy of an extreme event. *J. Climate*, **26,** 2811–2832, doi: 10.1175/JCLI-D-12-00270.1.

Isard, S. A., J. R. Angel, and G. T. VanDyke, 2000: Zones of origin for Great Lakes cyclones in North America, 1899–1996. *Mon. Wea. Rev.*, **128,** 474–485, doi: 10.1175/1520-0493(2000)128<0474:ZOOFGL>2.0.CO;2.

Jaffe, S. C., J. E. Martin, D. J. Vimont, and D. J. Lorenz, 2011: A synoptic climatology of episodic, subseasonal retractions of the Pacific jet. *J. Climate*, **24**, 2846–2860, doi: 10.1175/2010JCLI3995.1.

Kenyon, J., and G. C. Hegerl, 2008: Influence of modes of climate variability on global temperature extremes. *J. Climate*, **21,** 3872–3889, doi: 10.1175/2008JCLI2125.1.

Konrad, C. E., II, 1996: Relationships between the intensity of cold-air outbreaks and the evolution of synoptic and planetary-scale features over North America. *Mon. Wea. Rev.*, **124,** 1067–1083, doi: 10.1175/1520-0493(1996)124<1067:RBTIOC>2.0.CO;2.

Konrad, C. E., II, and S. J. Colucci, 1989: An examination of extreme cold air outbreaks over eastern North America. *Mon. Wea. Rev.*, **117,** 2687–2700, doi: 10.1175/1520-0493(1989)117<2687:AEOECA>2.0.CO;2.

Lim, Y.-K., and S. D. Schubert, 2011: The impact of ENSO and the Arctic Oscillation on winter temperature extremes in the southeast United States. *Geophys. Res. Lett.*, **38,** L15706, doi: 10.1029/2011GL048283.

Loikith, P. C., and A. J. Broccoli, 2012: Characteristics of observed atmospheric circulation patterns associated with temperature extremes over North America. *J. Climate*, **25,** 7266–7281, doi: 10.1175/JCLI-D-11-00709.1.

Loikith, P. C., and A. J. Broccoli, 2014: The influence of recurrent modes of climate variability on the occurrence of winter and summer extreme temperatures over North America. *J. Climate*, **27,** 1600–1618, doi: 10.1175/JCLI-D-13-00068.1.

Loikith, P. C., B. R. Lintner, and A. Sweeney, 2017: Characterizing large-scale meteorological patterns and associated temperature and precipitation extremes over the northwestern United States using self-organizing maps. *J. Climate*, **30,** 2829–2847, doi: 10.1175/JCLI-D-16-0670.1.

Madonna, E., H. Wernli, H. Joos, and O. Martius, 2014: Warm conveyor belts in the ERA-Interim dataset (1979–2010). Part I: Climatology and potential vorticity evolution. *J. Climate*, **27,** 3–26, doi: 10.1175/JCLI-D-12-00720.1.

Massacand, A. C., H. Wernli, and H. C. Davies, 2001: Influence of upstream diabatic heating upon an alpine event of heavy precipitation. *Mon. Wea. Rev.*, **129**, 2822–2828, doi: 10.1175/1520-0493(2001)129<2822:IOUDHU>2.0.CO;2.

Matsueda, S., and Y. Takaya, 2015: Global influence of the Madden–Julian Oscillation on extreme temperature events. *J. Climate*, **28,** 4141–4151, doi: 10.1175/JCLI-D-14-00625.1.

Meehl, G. A., and C. Tebaldi, 2004: More intense, more frequent, and longer lasting heat waves in the 21st century. *Science*, **305,** 994–997, doi: 10.1126/science.1098704.

Meehl, G. A., C. Tebaldi, H. Teng, and T. C. Peterson, 2007: Current and future U.S. weather extremes and El Niño. *Geophys. Res. Lett.*, **34,** L20704, doi: 10.1029/2007GL031027.

Moore, B. J., 2017: Rossby wave breaking and widespread extreme precipitation events in the central and eastern U.S. Ph.D. Dissertation, University at Albany, SUNY, 188 pp.

Moore, B. J., K. M. Mahoney, E. M. Sukovich, R. Cifelli, and T. M. Hamill, 2015: Climatology and environmental characteristics of extreme precipitation events in the southeastern United States. *Mon. Wea. Rev.*, **143,** 718–741, doi: 10.1175/MWR-D-14-00065.1.

Mundhenk, B. D., E. A. Barnes, and E. D. Maloney, 2016: All-season climatology and variability of atmospheric river frequencies over the North Pacific. *J. Climate*, **29,** 4885–4903, doi: 10.1175/JCLI-D-15-0655.1.

Namias, J., 1978: Multiple causes of the North American abnormal winter 1976–77. *Mon. Wea. Rev.*, **106,** 279–295, doi: 10.1175/1520-0493(1978)106<0279:MCOTNA>2.0.CO;2.

NWS, 2018: NWS Weather Fatality, Injury, and Damage Statistics. Accessed 27 August 2018, http://www.nws.noaa.gov/om/hazstats.shtml.

Neiman, P. J., F. M. Ralph, G. A. Wick, J. D. Lundquist, and M. D. Dettinger, 2008: Meteorological characteristics and overland precipitation impacts of atmospheric rivers affecting the west coast of North America based on eight years of SSM/I satellite observations. *J. Hydrometeor.*, **9,** 22–47, doi: 10.1175/2007JHM855.1.

North, G. R., T. L. Bell, R. F. Cahalan, and F. J. Moeng, 1982: Sampling errors in the estimation of empirical orthogonal functions. *Mon. Wea. Rev.*, **110**, 699–706, doi: 10.1175/1520-0493(1982)110<0699:SEITEO>2.0.CO;2.

Peterson, T. C., M. P. Hoerling, P. A. Stott, and S. C. Herring, 2013: Explaining extreme events of 2012 from a climate perspective. *Bull. Amer. Meteor. Soc.*, **94,** S1–S74, doi: 10.1175/BAMS-D-13-00085.1.

Peterson, A. G., and J. T. Abatzoglou, 2014: Observed changes in false springs over the contiguous United States. *Geophys. Res. Lett.*, **41,** 2156–2162, doi: 10.1002/2014GL059266.

Pfahl, S., C. Schwierz, M. Croci-Maspoli, C. M. Grams, and H. Wernli, 2015: Importance of latent heat release in ascending air streams for atmospheric blocking. *Nat. Geosci.*, **8**, 610–614, doi: 10.1038/ngeo2487.

Portis, D. H., M. P. Cellitti, W. L. Chapman, and J. E. Walsh, 2006: Low-frequency variability and evolution of North American cold air outbreaks. *Mon. Wea. Rev.*, **134,** 579–597, doi: 10.1175/MWR3083.1.

Ralph, F. M., P. J. Neiman, and G. A. Wick, 2004: Satellite and CALJET aircraft observations of atmospheric rivers over the eastern North Pacific Ocean during the winter of 1997/98.

Mon. Wea. Rev., **132,** 1721–1745, doi: 10.1175/1520-0493(2004)132<1721:SACAOO>2.0.CO;2.

Rex, D. F., 1950: Blocking action in the middle troposphere and its effect upon regional climate. I: An aerological study of blocking action. *Tellus*, **2A,** 196–211, doi: 10.1111/j.2153-3490.1950.tb00331.x.

Riemer, M., S. C. Jones, and C. A. Davis, 2008: The impact of extratropical transition on the downstream flow: An idealized modelling study with a straight jet. *Quart. J. Roy. Meteor. Soc.*, **134**, 69–91, doi: 10.1002/qj.189.

Rogers, J. C., and R. V. Rohli, 1991: Florida citrus freezes and polar anticyclones in the Great Plains. *J. Climate*, **4,** 1103–1113, doi: 10.1175/1520-0442(1991)004<1103:FCFAPA>2.0.CO;2.

Roundy, P. E., N. Sakaeda, K. MacRitchie, and L. Gloeckler, 2017: Weather-climate interactions and MJO influences. *Climate Extremes: Patterns and Mechanisms*, S.-Y. S. Wang, J.-H. Yoon, C. C. Funk, and R. R. Gillies, Eds., American Geophysical Union, 139–163, doi: 10.1002/9781119068020.ch9.

Saha, S., and Coauthors, 2010: The NCEP Climate Forecast System Reanalysis. *Bull. Amer. Meteor. Soc.*, **91**, 1015–1057, doi: 10.1175/2010BAMS3001.1.

Saha, S., and Coauthors, 2014: The NCEP Climate Forecast System version 2. *J. Climate*, **27**, 2185–2208, doi: 10.1175/JCLI-D-12-00823.1.

Sanders, F. and J. R. Gyakum, 1980, Synoptic-dynamic climatology of the "bomb." *Mon. Wea. Rev.*, **108,** 1589–1606, doi: 10.1175/1520-0493(1980)108<1589:SDCOT>2.0.CO;2.

Scherer, M., and N. S. Diffenbaugh, 2014: Transient twenty-first century changes in daily-scale temperature extremes in the United States. *Climate Dyn.*, **42,** 1383–1404, doi: 10.1007/s00382-013-1829-2.

Thompson, D. W. J., and J. M. Wallace, 1998: The Arctic oscillation signature in wintertime geopotential height and temperature fields. *Geophys. Res. Lett.*, **25,** 1297–1300, doi: 10.1029/98GL00950.

Tippett, M. K., J. T. Allen, V. A. Gensini, and H. E. Brooks, 2015: Climate and hazardous convective weather. *Curr. Climate Change Rep.*, **1,** 60–73, doi: 10.1007/s40641-015-0006-6.

Torn, R. D., 2010: Diagnosis of the downstream ridging associated with extratropical transition using short-term ensemble forecasts. *J. Atmos. Sci.*, **67**, 817–833, doi: 10.1175/2009JAS3093.1.

Torn, R. D., and G. J. Hakim, 2015: Comparison of wave packets associated with extratropical transition and winter cyclones. *Mon. Wea. Rev.*, **143**, 1782–1803, doi: 10.1175/MWR-D-14-00006.1.

Turner, J. K., and J. R. Gyakum, 2011: The development of arctic air masses in northwest Canada and their behavior in a warming climate. *J. Climate*, **24,** 4618–4633, doi: 10.1175/2011JCLI3855.1.

Vavrus, S., J. E. Walsh, W. L. Chapman, and D. Portis, 2006: The behavior of extreme cold air outbreaks under greenhouse warming. *Int. J. Climatol.*, **26,** 1133–1147, doi: 10.1002/joc.1301.

Walsh, J. E., A. S. Phillips, D. H. Portis, and W. L. Chapman, 2001: Extreme cold outbreaks in the United States and Europe, 1948–99. *J. Climate*, **14,** 2642–2658, doi: 10.1175/1520-0442(2001)014<2642:ECOITU>2.0.CO;2.

Wheeler, M. C., and H. H. Hendon, 2004: An all-season real-time multivariate MJO index: Development of an index for monitoring and prediction. *Mon. Wea. Rev.*, **132,** 1917–1932, doi: 10.1175/1520-0493(2004)132<1917:AARMMI>2.0.CO;2.

Wilks, D. S., 2011: Statistical Methods in the Atmospheric Sciences. 3rd ed. Elsevier, 676 pp.

Winters, A. C., D. Keyser, and L. F. Bosart, 2018: The development of the North Pacific Jet Phase Diagram as an objective tool to monitor the state of the upper-tropospheric flow pattern. *Wea. Forecasting*, **33,** (in review).

Westby, R. M., Y.-Y. Lee, and R. X. Black, 2013: Anomalous temperature regimes during the cool season: Long-term trends, low-frequency mode modulation, and representation in CMIP5 simulations. *J. Climate*, **26,** 9061–9076, doi: 10.1175/JCLI-D-13-00003.1.

Westby, R. M., and R. X. Black, 2015: Development of anomalous temperature regimes over the southeastern United States: Synoptic behavior and role of low-frequency modes. *Wea. Forecasting*, **30,** 553–570, doi: 10.1175/WAF-D-14-00093.1.

Wolter, K., M. Hoerling, J. K. Eischeid, G. J. van Oldenborgh, X.-W. Quan, J. E. Walsh, T. N. Chase, and R. M. Dole, 2015: How unusual was the cold winter of 2013/14 in the Upper Midwest? *Bull. Amer. Meteor. Soc.*, **96,** S10–S14, doi: 10.1175/BAMS-D-15-00126.1.

Xie, Z., R. X. Black, and Y. Deng, 2017: Daily-scale planetary wave patterns and the modulation of cold season weather in the northern extratropics. *J. Geophys. Res. Atmos.*, **122,** 8383–8398, doi: 10.1002/2017JD026768.

Zhang, C., 2016: MJO and extreme weather/climate events. *Dynamics and Predictability of Large-Scale, High-Impact Weather and Climate Events*, J. Li, R. Swinbank, R. Grotjahn, and H. Volkert, Eds., Cambridge University Press, 294–300, doi: 10.1017/CBO9781107775541.025.

Zhu, Y., and R. E. Newell, 1998: A proposed algorithm for moisture fluxes from atmospheric rivers. *Mon. Wea. Rev.*, **126,** 725–735, doi: 10.1175/1520-0493(1998)126<0725:APAFMF>2.0.CO;2.

Table Captions

TABLE 1. Selected studies that have sought relationships between cool season ETEs and modes of intraannual and interannual climate variability.

TABLE 2. The characteristics of continental U.S. ETEs identified during the 36-year period, 1979–2014. The characteristics provided include the minimum gridpoint thresholds required for the identification of an ETE within the eastern and western U.S. domains, the total number of ETEs identified within the eastern and western U.S. domains, and the number of ETEs that occurred during the cool season. Refer to the text for a full discussion of the ETE identification scheme.

Tables

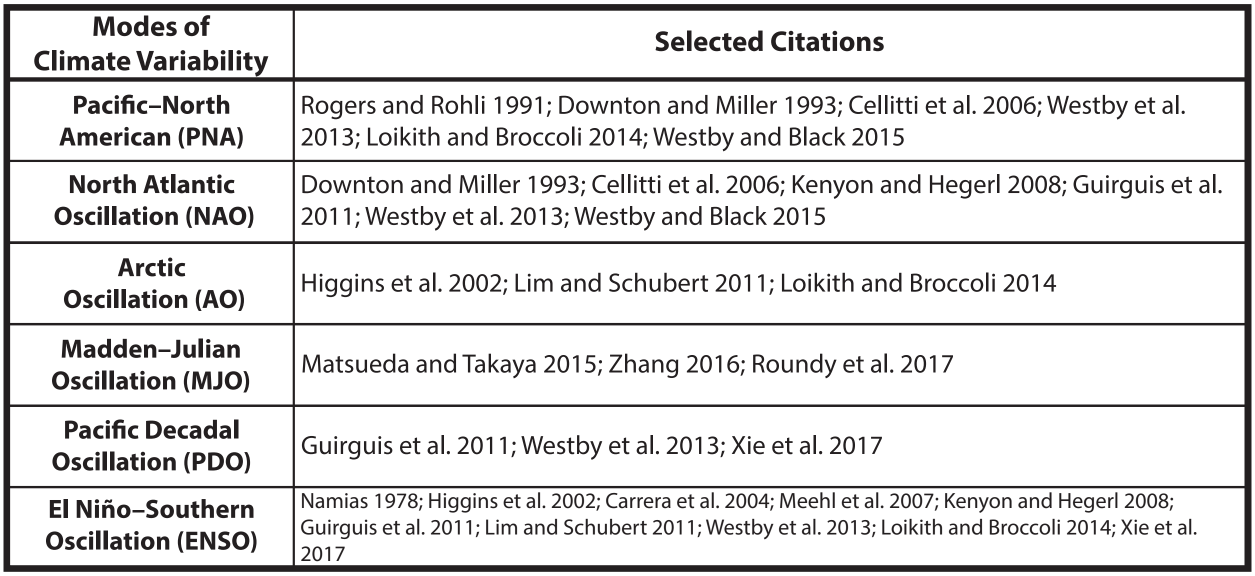

Modes of Climate Variability	Selected Citations
Pacific–North American (PNA)	Rogers and Rohli 1991; Downton and Miller 1993; Cellitti et al. 2006; Westby et al. 2013; Loikith and Broccoli 2014; Westby and Black 2015
North Atlantic Oscillation (NAO)	Downton and Miller 1993; Cellitti et al. 2006; Kenyon and Hegerl 2008; Guirguis et al. 2011; Westby et al. 2013; Westby and Black 2015
Arctic Oscillation (AO)	Higgins et al. 2002; Lim and Schubert 2011; Loikith and Broccoli 2014
Madden–Julian Oscillation (MJO)	Matsueda and Takaya 2015; Zhang 2016; Roundy et al. 2017
Pacific Decadal Oscillation (PDO)	Guirguis et al. 2011; Westby et al. 2013; Xie et al. 2017
El Niño–Southern Oscillation (ENSO)	Namias 1978; Higgins et al. 2002; Carrera et al. 2004; Meehl et al. 2007; Kenyon and Hegerl 2008; Guirguis et al. 2011; Lim and Schubert 2011; Westby et al. 2013; Loikith and Broccoli 2014; Xie et al. 2017

TABLE 1. Selected studies that have sought relationships between cool season ETEs and modes of intraannual and interannual climate variability.

Extreme Temperature Events				
	Spatial Domain	Min. Gridpoint Threshold	Total Number of Identified Events	Cool Season Events
Extreme Warm Events	**East**	224	304	239
	West	144	264	204
Extreme Cold Events	**East**	221	225	173
	West	125	269	196

TABLE 2. The characteristics of continental U.S. ETEs identified during the 36-year period, 1979–2014. The characteristics provided include the minimum gridpoint thresholds required for the identification of an ETE within the eastern and western U.S. domains, the total number of ETEs identified within the eastern and western U.S. domains, and the number of ETEs that occurred during the cool season. Refer to the text for a full discussion of the ETE identification scheme.

Figure Captions

FIG. 1. (a) Frequency distribution of 2-m temperatures compiled at 24-h intervals within a 21-day window centered on 1900 UTC 30 May for every year between 1979 and 2014 for a grid point near Albany, NY (43°N; 74°W). The vertical black bar identifies the 99th-percentile temperature of the distribution and the quantity in the top left of the panel indicates the total number of 1-h forecasts that are used to construct the distribution. (b) 99th-percentile temperature at 1900 UTC 30 May is shaded in the fill pattern. The black boxes identify the eastern and western U.S. domains used to identify continental U.S. ETEs. (c) Frequency distribution of the number of grid points characterized by extreme warmth within the subset of 1-h forecasts during 1979–2014 that exhibit at least one grid point over land in the eastern U.S. domain with a 2-m temperature greater than its respective 99th-percentile temperature. The vertical black bar identifies the number of grid points corresponding to the 95th percentile of the distribution. The black arrow identifies the maximum number of grid points characterized by extreme warmth in a single 1-h forecast during 1979–2014.

FIG. 2. (a) The number of extreme warm events that initiate within the eastern U.S. domain is shaded in the fill pattern. Individual extreme warm event centroids are represented by dots and are colored according to their respective geographic cluster. (b) As in (a), but for extreme warm events that initiate within the western U.S. domain.

FIG. 3. As in Fig. 2, but for extreme cold events that initiate within the (a) eastern U.S. domain and (b) western U.S. domain.

FIG. 4. (a) September–May 250-hPa mean zonal wind is contoured in black every 10 m s^{-1} above 30 m s^{-1}, and the regression of 250-hPa zonal wind anomaly data onto standardized PC 1 (i.e., EOF 1) is shaded in m s^{-1}. The variance of 250-hPa zonal wind during the cool season that is explained by EOF 1 is listed in the top right of the panel. (b) As in (a), but for the regression of 250-hPa zonal wind anomaly data onto standardized PC 2 (i.e., EOF 2). Figure and caption from Winters et al. (2018).

FIG. 5. Schematic illustrating the NPJ Phase Diagram and the classification scheme used to determine the NPJ regime prior to ETE initiation.

FIG. 6. Composite mean 250-hPa wind speed in m s^{-1} is shaded in the fill pattern, 250-hPa geopotential height is contoured in black every 120 m, and 250-hPa geopotential height anomalies are contoured in solid red and dashed blue every 30 m for positive and negative values, respectively, 4 days following the initiation of (a) a jet extension, (b) a jet retraction, (c) a poleward shift, and (d) an equatorward shift regime. The numbers in the bottom right of each panel indicate the number of cases included in each composite and stippled areas represent locations where the 250-hPa geopotential height anomalies are statistically significantly different from climatology at the 99% confidence level. Figure and caption from Winters et al. (2018).

FIG. 7. Composite anomalies of mean sea-level pressure are contoured in solid and dashed black every 2 hPa for positive and negative values, respectively, and 850-hPa temperature anomalies are shaded in the fill pattern every 1 K 4 days following the initiation of (a) a jet extension, (b) a jet retraction, (c) a poleward shift, and (d) an equatorward shift regime. The numbers in the

bottom right of each panel indicate the number of cases included in each composite and stippled areas represent locations where the 850-hPa temperature anomalies are statistically significantly different from climatology at the 99% confidence level. Figure and caption from Winters et al. (2018).

FIG. 8. (a) The number of eastern U.S. extreme warm events during the cool season (Sep–May), fall (Sep–Nov), winter (Dec–Feb), and spring (Mar–May) associated with each NPJ regime during the 3–7-day period prior to event initiation. The quantities listed above each bar indicate the number of events that are associated with a particular NPJ regime. As in (a), but for (b) Northern Plains, (c) Southern Plains, and (d) East Coast extreme warm events.

FIG. 9. As in Fig. 8, but for (a) western U.S., (b) Pacific Northwest, (c) Northern Rockies, and (d) Southwest extreme warm events.

FIG. 10. (a) Composite trajectory showing the evolution of the NPJ at 6-h intervals during the 10-day period prior to ETE initiation for all eastern U.S. extreme warm events and for extreme warm events within the three eastern U.S. geographic clusters. All trajectories are colored by geographic cluster according to the legend and are shifted such that they begin at the origin of the NPJ Phase Diagram 10 days prior to ETE initiation. The colored diamonds offset from the origin of the NPJ Phase Diagram correspond to the end point of a particular trajectory and identify the average state of the NPJ at the time of ETE initiation. (b) As in (a), but for all western U.S. extreme warm events and for the extreme warm events within the three western U.S. geographic clusters.

FIG. 11. As in Fig. 8, but for (a) eastern U.S., (b) Northern Plains, (c) Northeast, (d) Southern Plains, and (e) Southeast extreme cold events.

FIG. 12. As in Fig. 8, but for (a) western U.S., (b) Pacific Northwest, (c) Northern Rockies, and (d) Southwest extreme cold events.

FIG. 13. As in Fig. 10, but for (a) eastern U.S. and (b) western U.S. extreme cold events.

FIG. 14. Composite synoptic-scale flow evolution prior to the initiation of a Southern Plains extreme warm event following a jet retraction. [left column] 250-hPa wind speed is shaded in m s^{-1} according to the legend, 250-hPa geopotential height is contoured in black every 12 dam, standardized 250-hPa geopotential height anomalies are contoured in solid and dashed yellow every 0.5σ for positive and negative values, respectively, and positive standardized precipitable water anomalies are shaded in green according to the legend (a) 6 days, (c) 4 days, (e) 2 days, and (g) 0 days prior to extreme warm event initiation. Stippled areas represent locations where the 250-hPa geopotential height anomalies are statistically significantly different from climatology at the 99% confidence level. [right column] Standardized 850-hPa temperature anomalies are shaded every 0.5σ according to the legend, mean sea level pressure is contoured in black every 4 hPa, and 1000–500-hPa thickness is contoured in dashed red and blue for values greater than 540 dam and less than or equal to 540 dam, respectively, (b) 6 days, (d) 4 days, (f) 2 days, and (h) 0 days prior to ETE initiation. The red 'L's and blue 'H's identify the locations of surface cyclones and anticyclones. Stippled areas represent locations where the 850-hPa

geopotential height anomalies are statistically significantly different from climatology at the 99% confidence level.

Figures

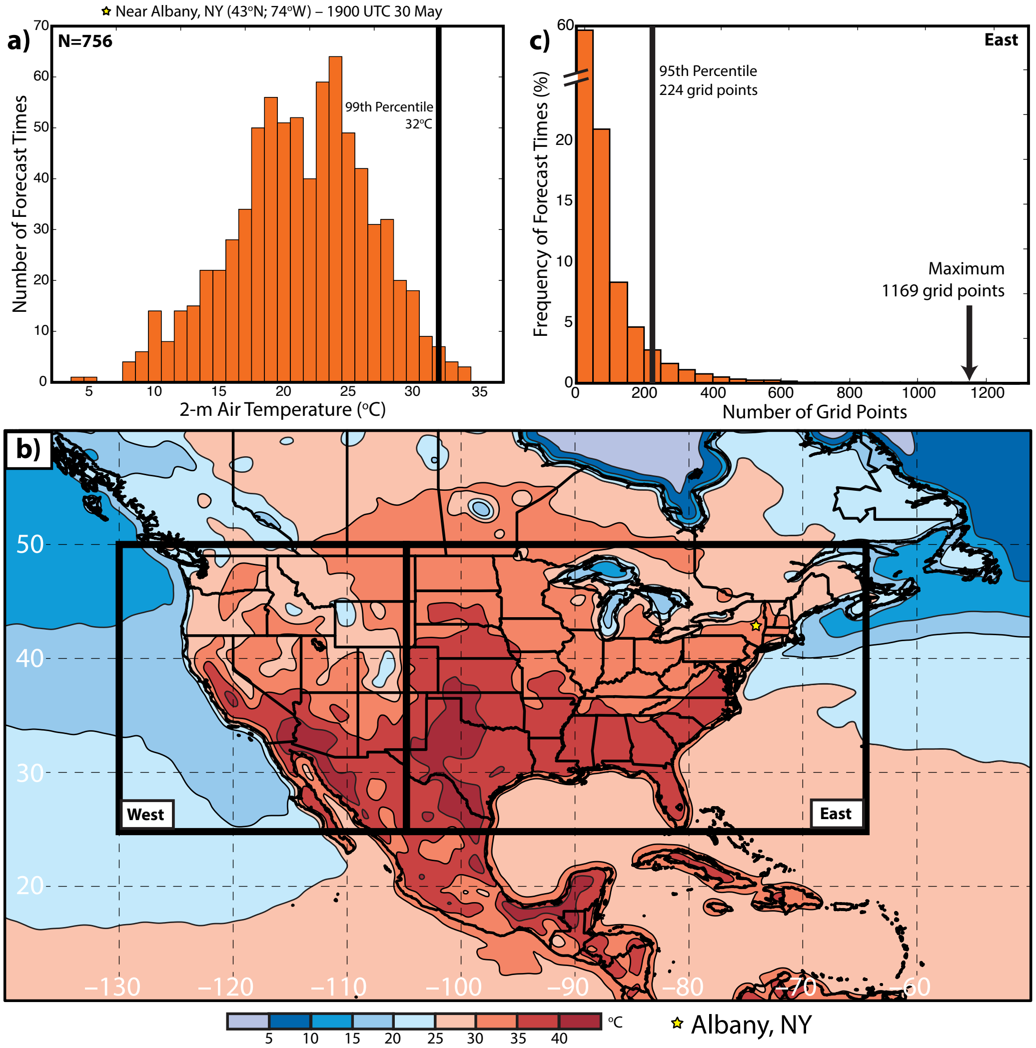

FIG. 1. (a) Frequency distribution of 2-m temperatures compiled at 24-h intervals within a 21-day window centered on 1900 UTC 30 May for every year between 1979 and 2014 for a grid point near Albany, NY (43°N; 74°W). The vertical black bar identifies the 99th-percentile temperature of the distribution and the quantity in the top left of the panel indicates the total number of 1-h forecasts that are used to construct the distribution. (b) 99th-percentile temperature at 1900 UTC 30 May is shaded in the fill pattern. The black boxes identify the eastern and western U.S. domains used to identify continental U.S. ETEs. (c) Frequency distribution of the number of grid points characterized by extreme warmth within the subset of 1-h forecasts during 1979–2014 that exhibit at least one grid point over land in the eastern U.S. domain with a 2-m temperature greater than its respective 99th-percentile temperature. The vertical black bar identifies the number of grid points corresponding to the 95th percentile of the distribution. The black arrow identifies the maximum number of grid points characterized by extreme warmth in a single 1-h forecast during 1979–2014.

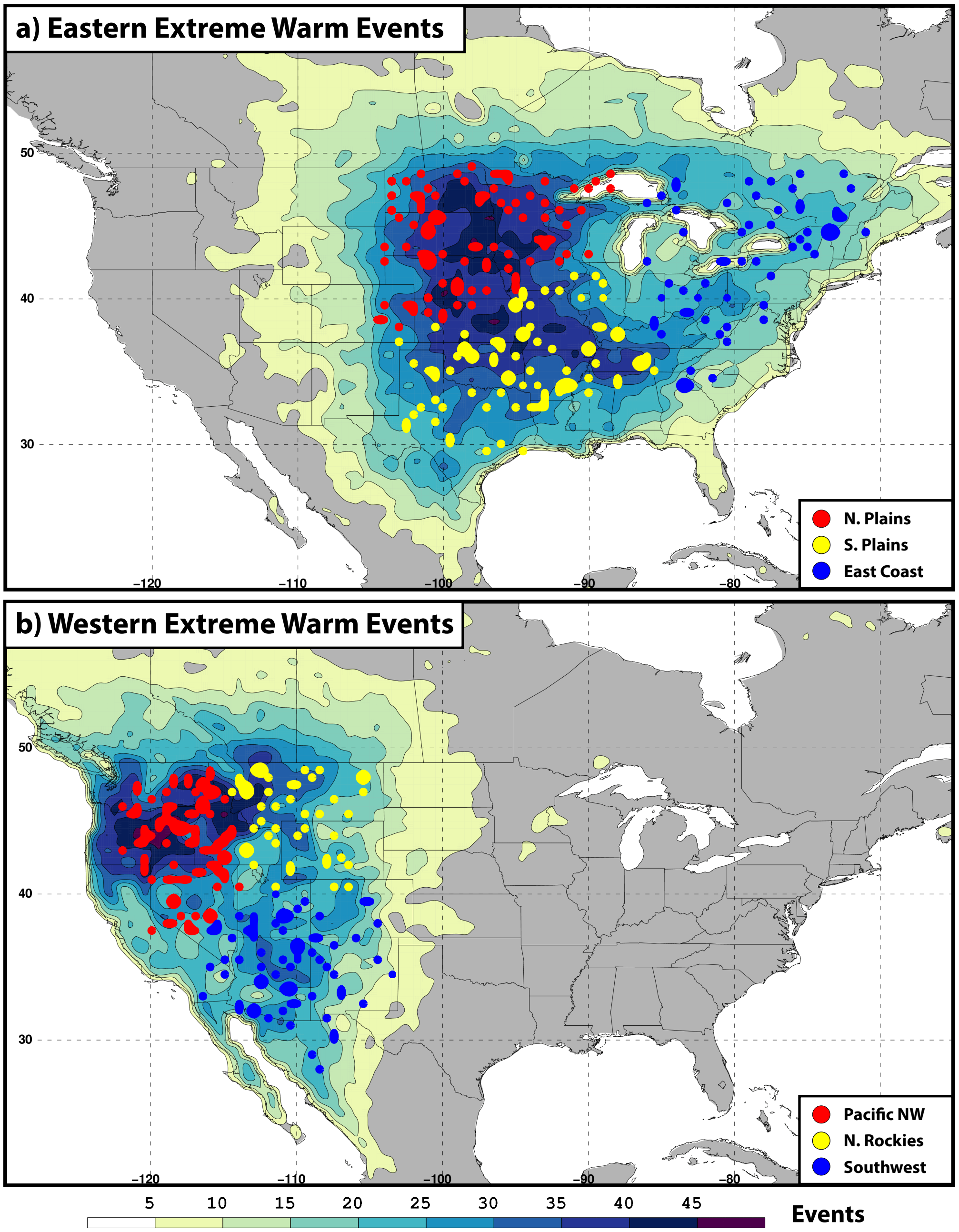

FIG. 2. (a) The number of extreme warm events that initiate within the eastern U.S. domain is shaded in the fill pattern. Individual extreme warm event centroids are represented by dots and are colored according to their respective geographic cluster. (b) As in (a), but for extreme warm events that initiate within the western U.S. domain.

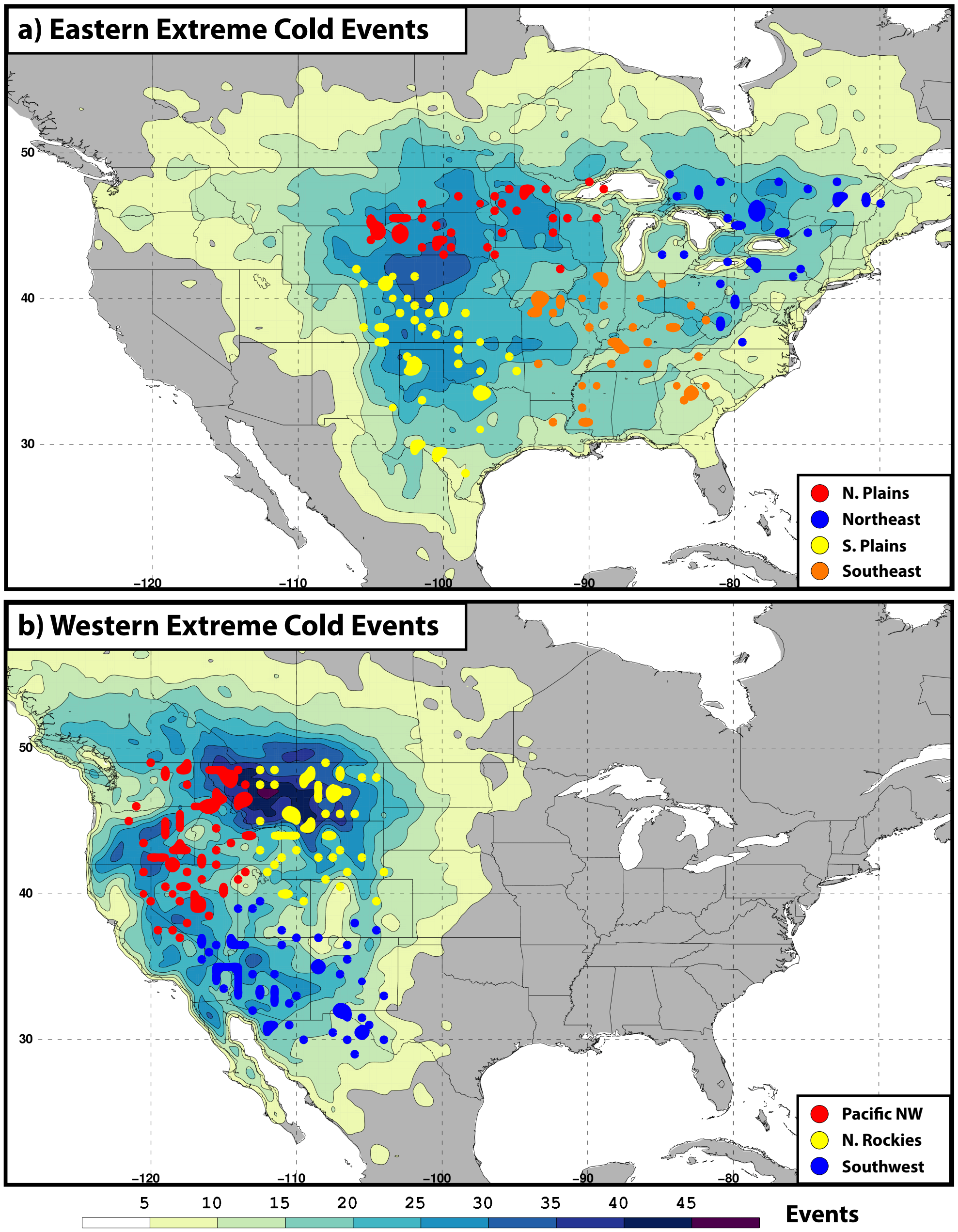

FIG. 3. As in Fig. 2, but for extreme cold events that initiate within the (a) eastern U.S. domain and (b) western U.S. domain.

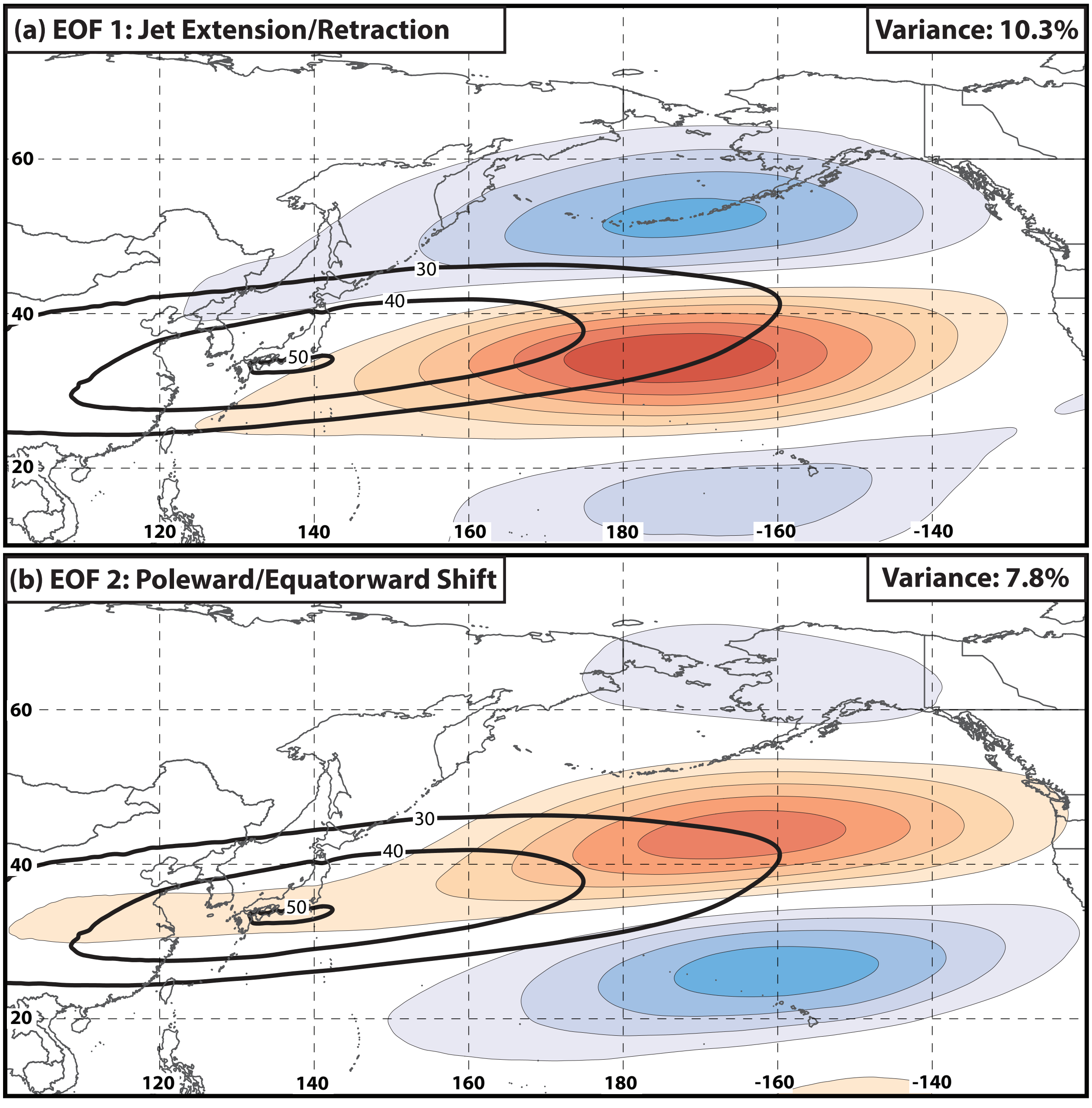

FIG. 4. (a) September–May 250-hPa mean zonal wind is contoured in black every 10 m s^{-1} above 30 m s^{-1}, and the regression of 250-hPa zonal wind anomaly data onto standardized PC 1 (i.e., EOF 1) is shaded in m s^{-1}. The variance of 250-hPa zonal wind during the cool season that is explained by EOF 1 is listed in the top right of the panel. (b) As in (a), but for the regression of 250-hPa zonal wind anomaly data onto standardized PC 2 (i.e., EOF 2). Figure and caption from Winters et al. (2018).

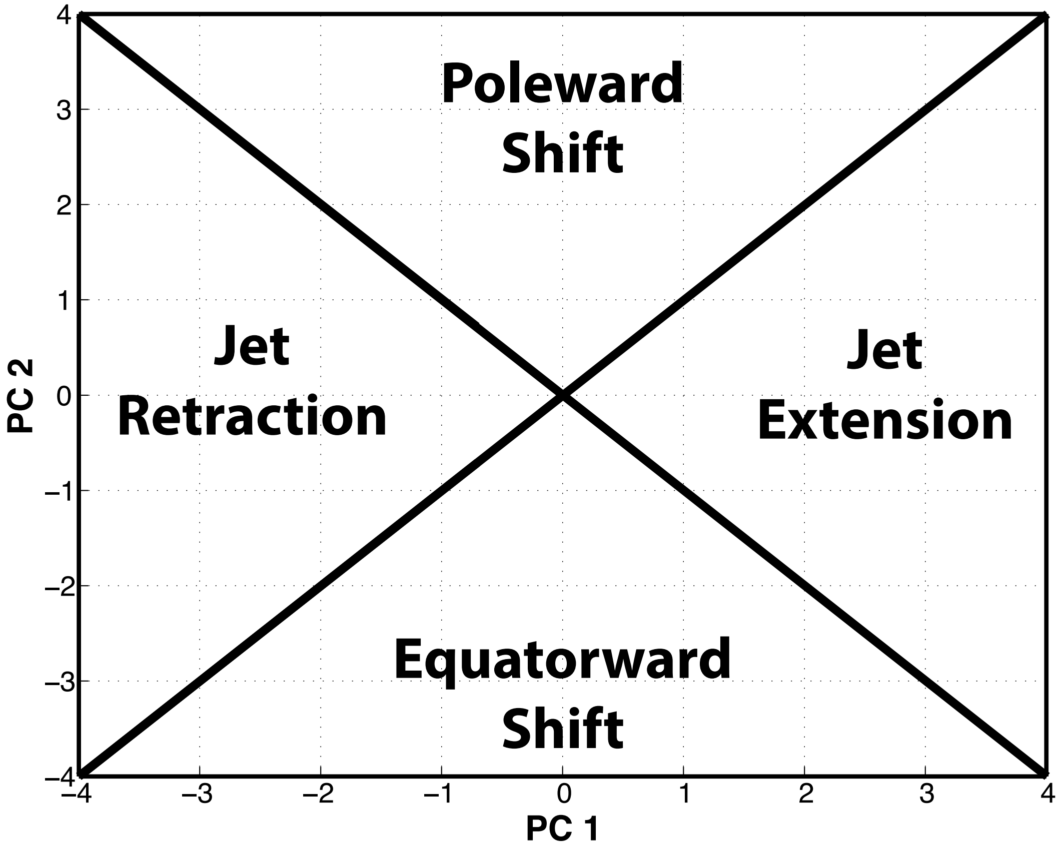

FIG. 5. Schematic illustrating the NPJ Phase Diagram and the classification scheme used to determine the NPJ regime prior to ETE initiation.

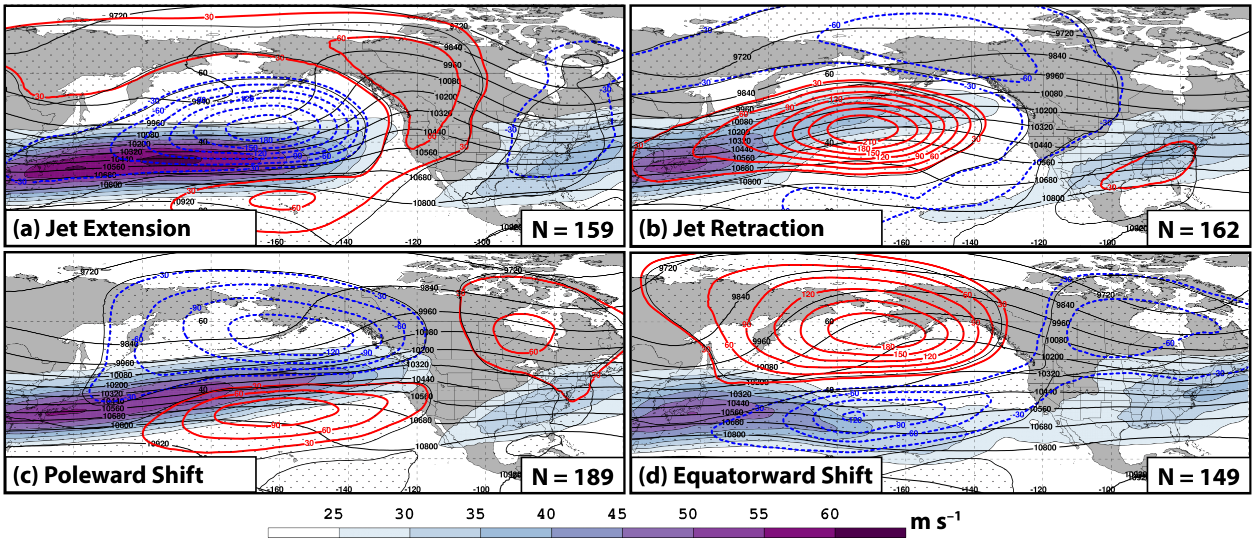

FIG. 6. Composite mean 250-hPa wind speed in m s^{-1} is shaded in the fill pattern, 250-hPa geopotential height is contoured in black every 120 m, and 250-hPa geopotential height anomalies are contoured in solid red and dashed blue every 30 m for positive and negative values, respectively, 4 days following the initiation of (a) a jet extension, (b) a jet retraction, (c) a poleward shift, and (d) an equatorward shift regime. The numbers in the bottom right of each panel indicate the number of cases included in each composite and stippled areas represent locations where the 250-hPa geopotential height anomalies are statistically significantly different from climatology at the 99% confidence level. Figure and caption from Winters et al. (2018).

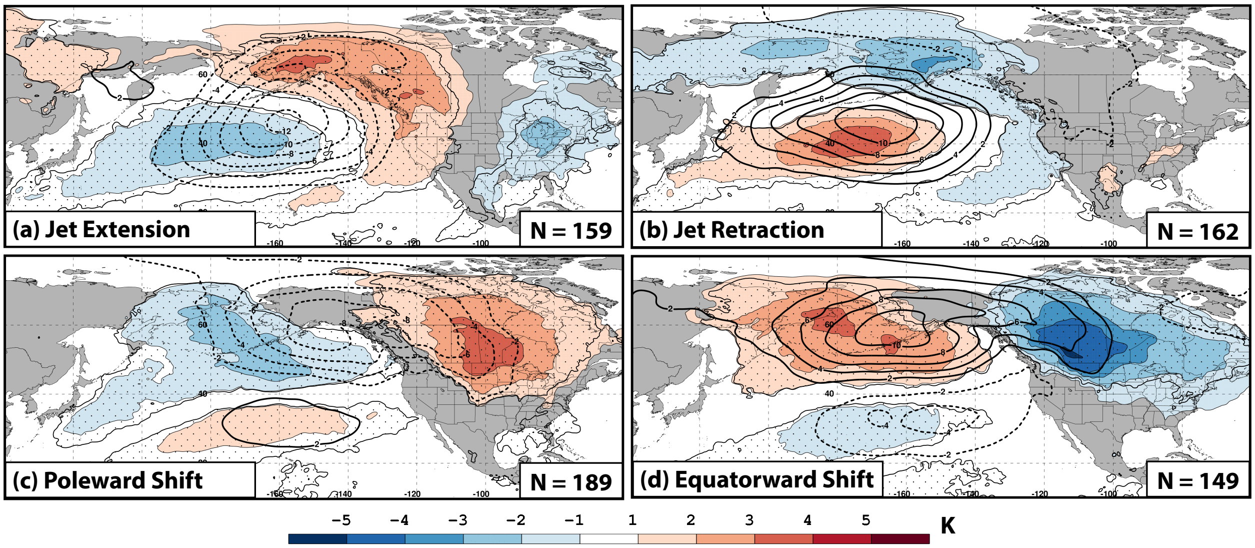

FIG. 7. Composite anomalies of mean sea-level pressure are contoured in solid and dashed black every 2 hPa for positive and negative values, respectively, and 850-hPa temperature anomalies are shaded in the fill pattern every 1 K 4 days following the initiation of (a) a jet extension, (b) a jet retraction, (c) a poleward shift, and (d) an equatorward shift regime. The numbers in the bottom right of each panel indicate the number of cases included in each composite and stippled areas represent locations where the 850-hPa temperature anomalies are statistically significantly different from climatology at the 99% confidence level. Figure and caption from Winters et al. (2018).

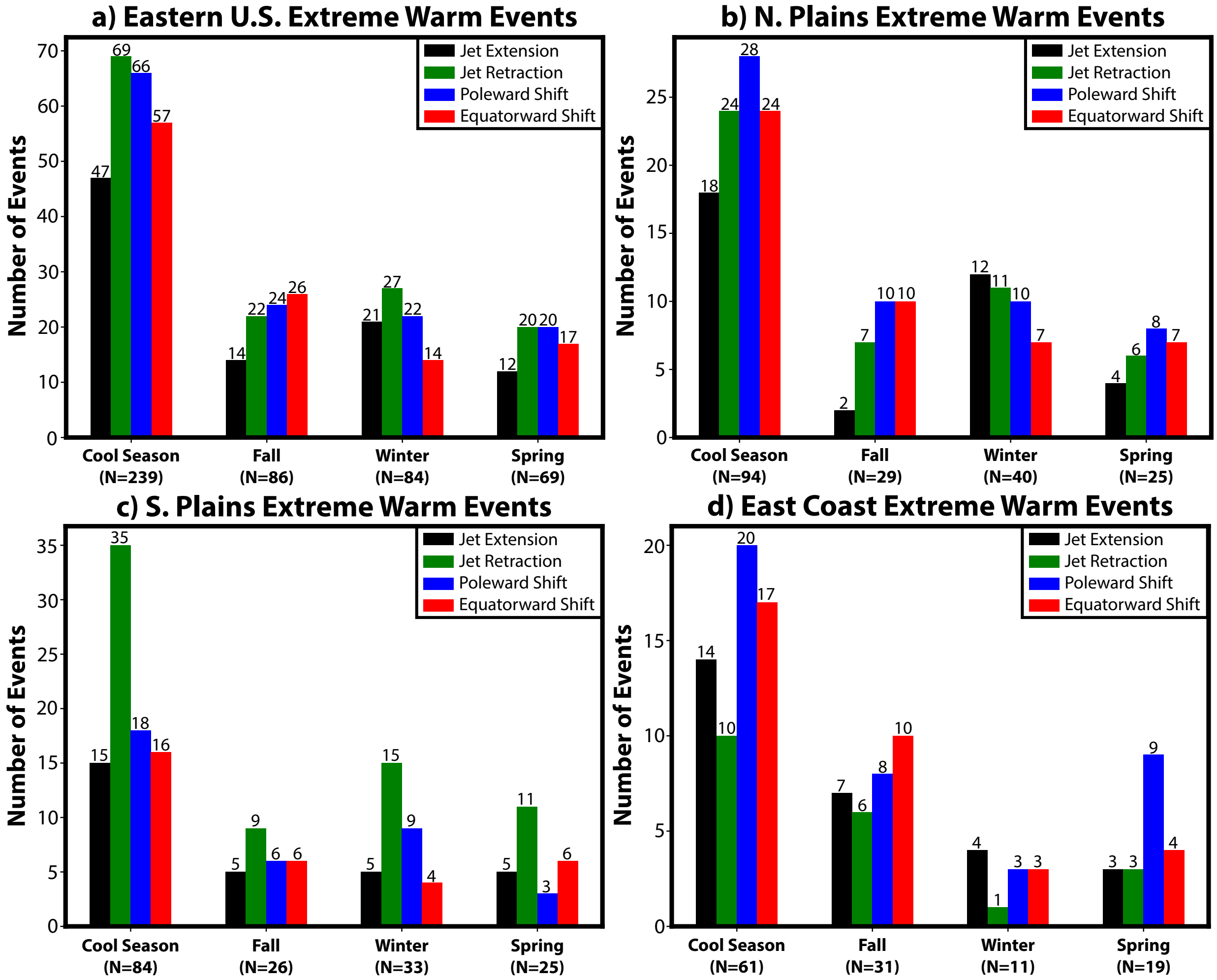

FIG. 8. (a) The number of eastern U.S. extreme warm events during the cool season (Sep–May), fall (Sep–Nov), winter (Dec–Feb), and spring (Mar–May) associated with each NPJ regime during the 3–7-day period prior to event initiation. The quantities listed above each bar indicate the number of events that are associated with a particular NPJ regime. As in (a), but for (b) Northern Plains, (c) Southern Plains, and (d) East Coast extreme warm events.

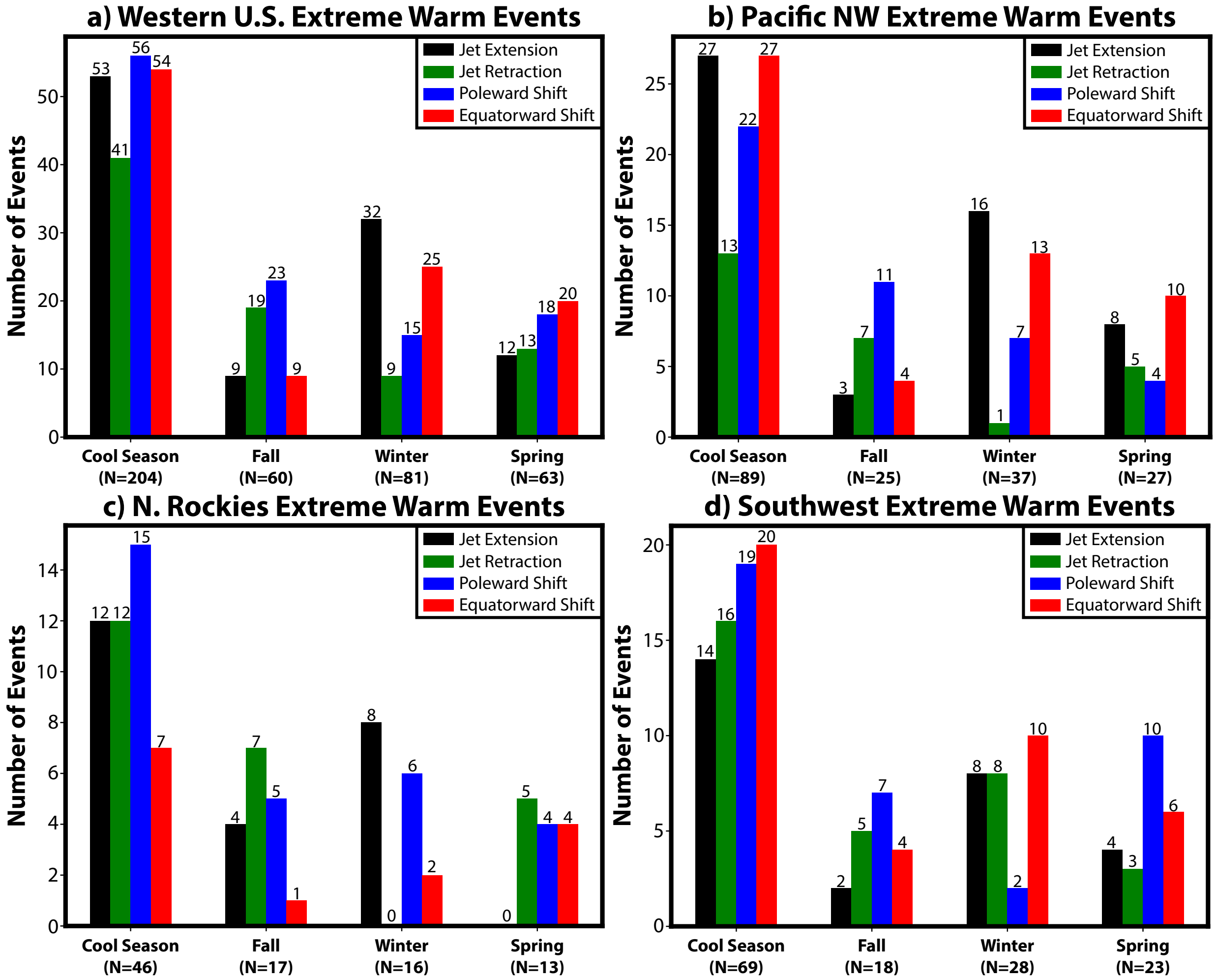

FIG. 9. As in Fig. 8, but for (a) western U.S., (b) Pacific Northwest, (c) Northern Rockies, and (d) Southwest extreme warm events.

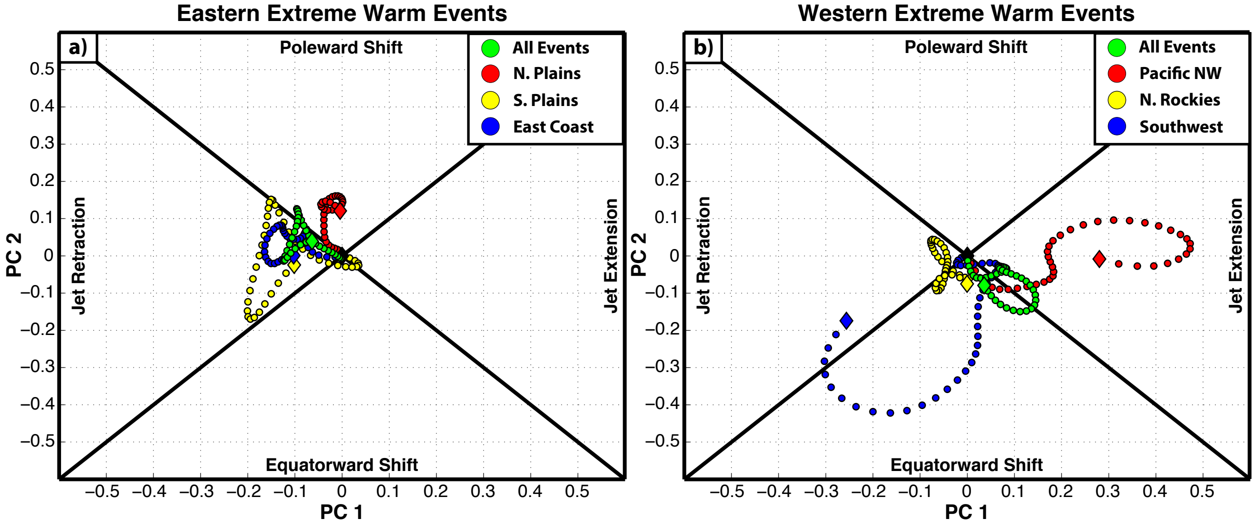

FIG. 10. (a) Composite trajectory showing the evolution of the NPJ at 6-h intervals during the 10-day period prior to ETE initiation for all eastern U.S. extreme warm events and for extreme warm events within the three eastern U.S. geographic clusters. All trajectories are colored by geographic cluster according to the legend and are shifted such that they begin at the origin of the NPJ Phase Diagram 10 days prior to ETE initiation. The colored diamonds offset from the origin of the NPJ Phase Diagram correspond to the end point of a particular trajectory and identify the average state of the NPJ at the time of ETE initiation. (b) As in (a), but for all western U.S. extreme warm events and for the extreme warm events within the three western U.S. geographic clusters.

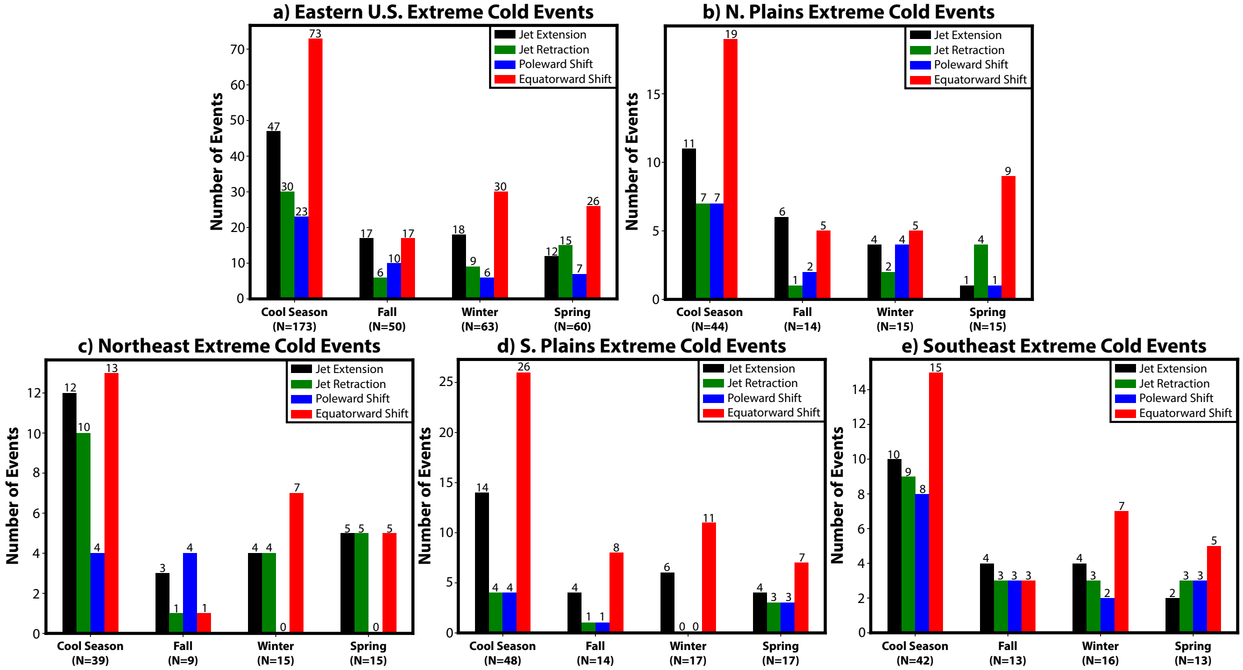

FIG. 11. As in Fig. 8, but for (a) eastern U.S., (b) Northern Plains, (c) Northeast, (d) Southern Plains, and (e) Southeast extreme cold events.

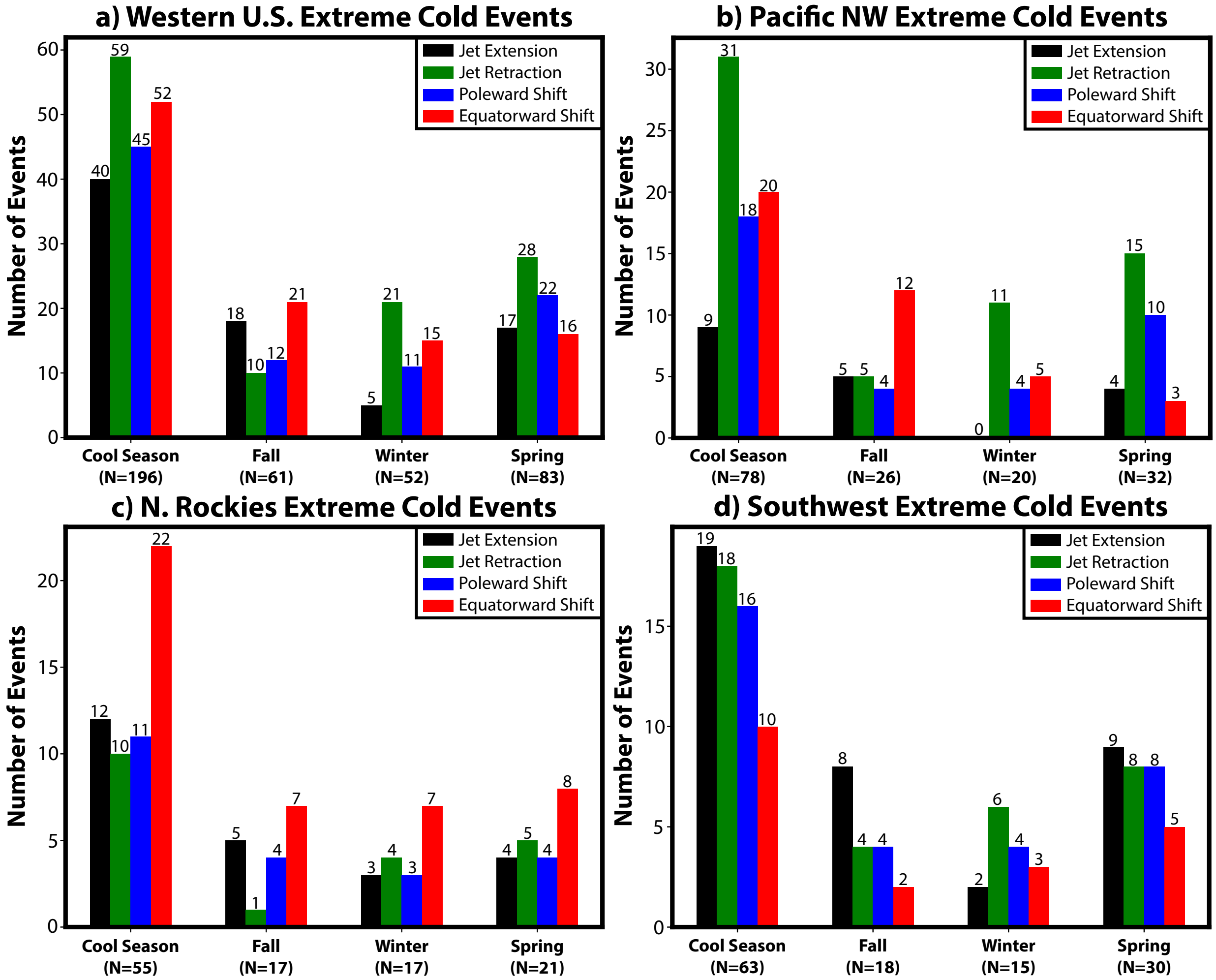

FIG. 12. As in Fig. 8, but for (a) western U.S., (b) Pacific Northwest, (c) Northern Rockies, and (d) Southwest extreme cold events.

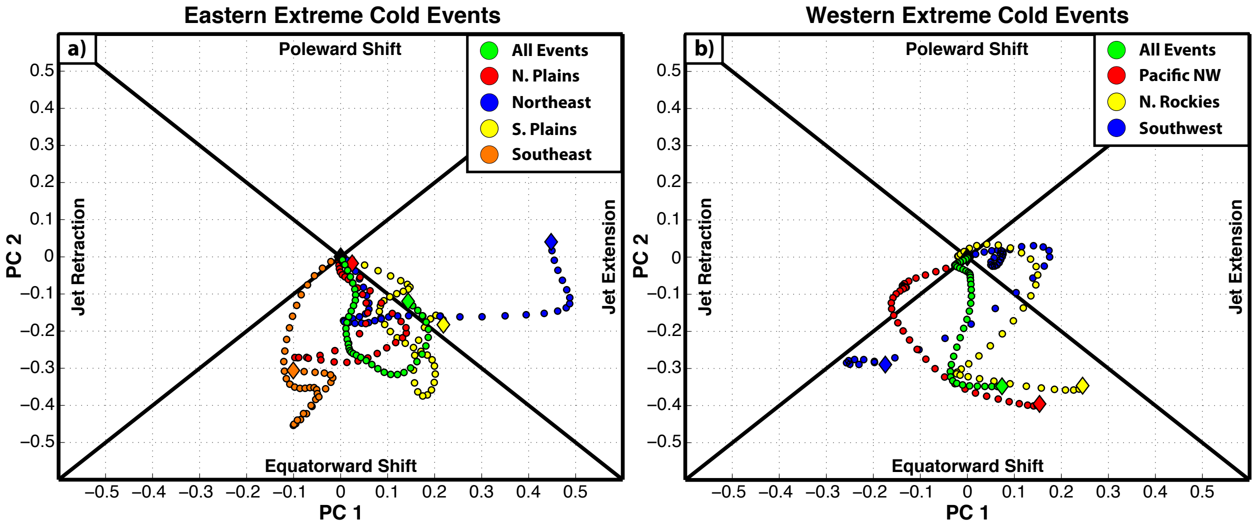

FIG. 13. As in Fig. 10, but for (a) eastern U.S. and (b) western U.S. extreme cold events.

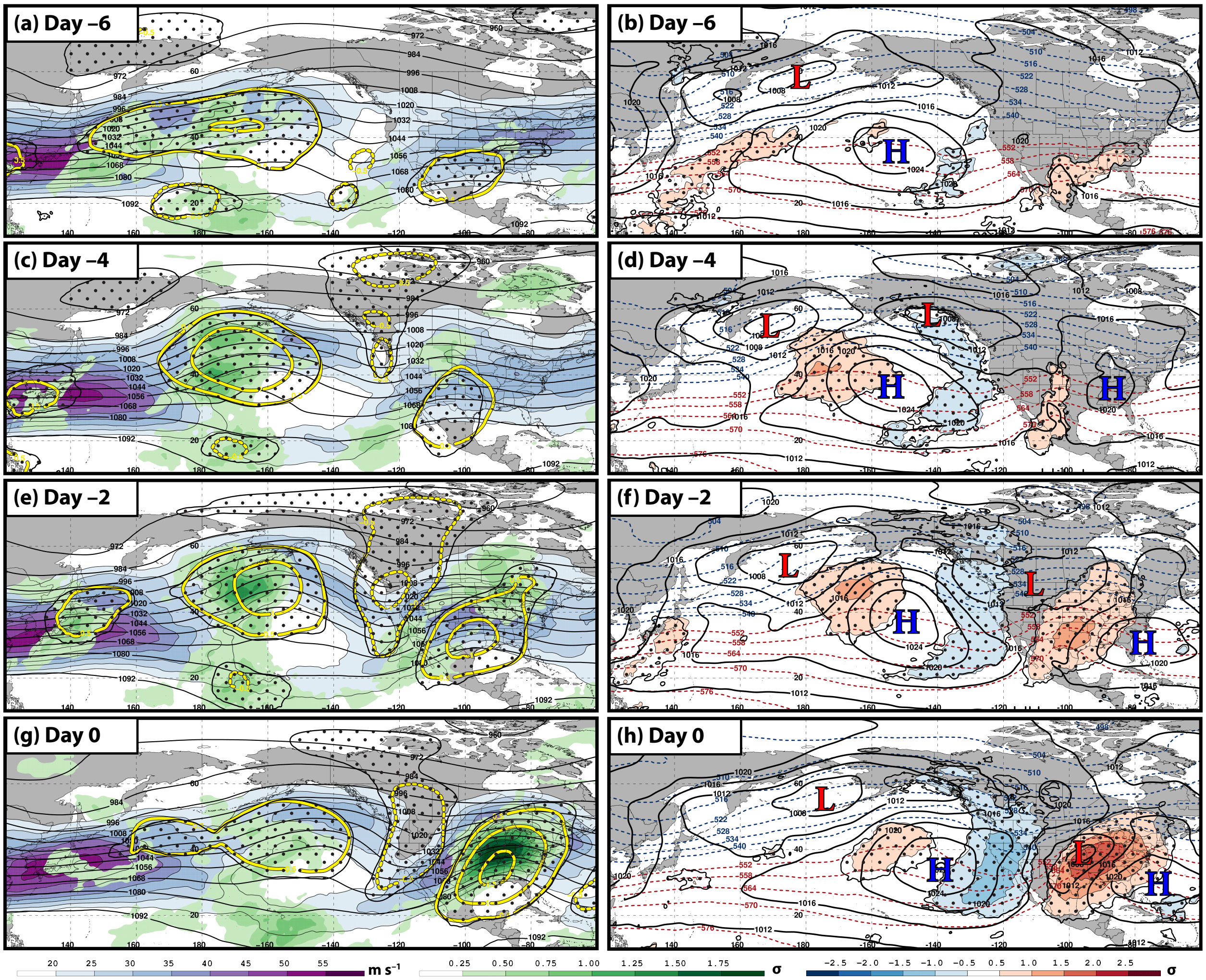

FIG. 14. Composite synoptic-scale flow evolution prior to the initiation of a Southern Plains extreme warm event following a jet retraction. [left column] 250-hPa wind speed is shaded in m s^{-1} according to the legend, 250-hPa geopotential height is contoured in black every 12 dam, standardized 250-hPa geopotential height anomalies are contoured in solid and dashed yellow every 0.5σ for positive and negative values, respectively, and positive standardized precipitable water anomalies are shaded in green according to the legend (a) 6 days, (c) 4 days, (e) 2 days, and (g) 0 days prior to extreme warm event initiation. Stippled areas represent locations where the 250-hPa geopotential height anomalies are statistically significantly different from climatology at the 99% confidence level. [right column] Standardized 850-hPa temperature anomalies are shaded every 0.5σ according to the legend, mean sea level pressure is contoured in black every 4 hPa, and 1000–500-hPa thickness is contoured in dashed red and blue for values greater than 540 dam and less than or equal to 540 dam, respectively, (b) 6 days, (d) 4 days, (f) 2 days, and (h) 0 days prior to ETE initiation. The red ‘L’s and blue ‘H’s identify the locations of surface cyclones and anticyclones. Stippled areas represent locations where the 850-hPa geopotential height anomalies are statistically significantly different from climatology at the 99% confidence level.